

ALMA OBSERVATIONS OF MOLECULAR CLOUDS IN THREE GROUP CENTERED ELLIPTICAL GALAXIES: NGC 5846, NGC 4636, AND NGC 5044

PASQUALE TEMI¹, ALEXANDRE AMBLARD^{1,2}, MYRIAM GITTI^{3,4}, FABRIZIO BRIGHENTI³, MASSIMO GASPARI^{5,6}, WILLIAM G. MATHEWS⁷, LAURENCE DAVID⁸

Draft version May 2, 2018

ABSTRACT

We present new ALMA CO(2–1) observations of two well studied group-centered elliptical galaxies: NGC 4636 and NGC 5846. In addition, we include a revised analysis of Cycle 0 ALMA observations of the central galaxy in the NGC 5044 group that has been previously published. We find evidence that molecular gas, in the form of off-center orbiting clouds, is a common presence in bright group-centered galaxies (BGG). CO line widths are $\gtrsim 10$ times broader than Galactic molecular clouds, and using the reference Milky Way X_{CO} , the total molecular mass ranges from as low as $2.6 \times 10^5 M_{\odot}$ in NGC 4636 to $6.1 \times 10^7 M_{\odot}$ in NGC 5044. With these parameters the virial parameters of the molecular structures is $\gg 1$. Complementary observations of NGC 5846 and NGC 4636 using the ALMA Compact Array (ACA) do not exhibit any detection of a CO diffuse component at the sensitivity level achieved by current exposures. The origin of the detected molecular features is still uncertain, but these ALMA observations suggest that they are the end product of the hot gas cooling process and not the result of merger events. Some of the molecular clouds are associated with dust features as revealed by HST dust extinction maps suggesting that these clouds formed from dust-enhanced cooling. The global nonlinear condensation may be triggered via the chaotic turbulent field or buoyant uplift. The large virial parameter of the molecular structures and correlation with the warm ($10^3 - 10^5 \text{K}$)/hot ($\geq 10^6$) phase velocity dispersion provide evidence that they are unbound giant molecular associations drifting in the turbulent field, consistently with numerical predictions of the chaotic cold accretion process. Alternatively, the observed large CO line widths may be generated by molecular gas flowing out from cloud surfaces due to heating by the local hot gas atmosphere.

Keywords: galaxies:groups:general - galaxies: elliptical and lenticular, cD - galaxies:individual (NGC 5044, NGC 5846, NGC 4636) - galaxies: ISM - galaxies: active

1. INTRODUCTION

Local brightest group galaxies (BGGs) are prime systems to study the physics of the hot interstellar or intergroup medium, including its connection with the central massive black hole and the associated active galactic nuclei (AGN) feedback. They are in many respects simple objects, where hot gas cooling and evolution can be investigated without other complicating processes like star formation or gas-rich merging (e.g., Feldmann et al. 2010; O’Sullivan et al. 2017).

In fact, the most massive group-centered elliptical galaxies have red and old stellar populations, with little or no evidence of recent star formation (Ziegler et al. 2005; van der Wel et al. 2005; Daddi et al. 2005; Werner et al. 2014; Gozaliasl et al. 2016). The three galaxies which we have selected for this study, NGC 4636, NGC 5044 and NGC 5846, are perfect example of passive systems, with very old stellar populations

(Trager et al. 2000; Annibali et al. 2006; Diniz et al. 2017) and star formation rates on the order of a few percent $M_{\odot} \text{yr}^{-1}$ (Werner et al. 2014).

Central galaxies in massive clusters have higher X-ray luminosities and are much richer in warm/cold interstellar medium (ISM), with molecular gas masses $M_{\text{H}_2} \sim 10^9 - 10^{11} M_{\odot}$ (Edge 2001; Salomé & Combes 2003; Pulido et al. 2017). However, they are located at distances ≥ 100 Mpc and usually inhabit complex environments – e.g., affected by merging, stripping, star formation, and supernovae – which make it difficult to fully unveil the gas cooling process and its connection to the feedback mechanism.

The absence or dearth of star formation in BGGs is remarkable. These galaxies usually have a massive hot gas halo radiating away $10^{41} - 10^{43} \text{erg s}^{-1}$ (Mathews & Brighenti 2003; Sun 2012; Goulding et al. 2016; Anderson et al. 2015). This corresponds to a cooling rate $\dot{M}_{\text{cool}} \sim 1 - 50 M_{\odot} \text{s}^{-1}$ if radiative losses are not balanced by some form of heating. Evidently, a continuous gas heating or removal mechanism is required to halt star formation. Since all these galaxies harbor supermassive black holes (SMBHs), it is natural to expect that the AGN feedback process plays a pivotal role in regulating the gas cooling (e.g., Croton et al. 2006; McNamara & Nulsen 2007; Gitti et al. 2012).

Indeed, *Chandra* and *XMM* observations have shown that hot gas ($T \sim 10^7 \text{K}$) cooling is suppressed by more than an order of magnitude with respect to the classical cooling flow expectation (e.g., McNamara & Nulsen 2007; Peterson et al. 2003; Peterson & Fabian 2006; McNamara & Nulsen 2012; Molendi et al. 2016). This is true at all mass scales,

¹ Astrophysics Branch, NASA Ames Research Center, Moffett Field, CA, USA

² BAER Institute, Sonoma, CA, USA

³ Physics and Astronomy Department, University of Bologna, Via Gobetti 93/2, 40129, Bologna, Italy

⁴ INAF, Istituto di Radioastronomia di Bologna, via Gobetti 101, 40129 Bologna, Italy

⁵ Department of Astrophysical Sciences, Princeton University, Princeton, NJ 08544, USA

⁶ *Einstein* and *Spitzer* Fellow

⁷ University of California Observatories/Lick Observatory, Department of Astronomy and Astrophysics, University of California, Santa Cruz, CA 95064, USA

⁸ Harvard-Smithsonian Center for Astrophysics, 60 Garden St., Cambridge, MA 02138, USA

from galaxies to clusters. X-ray images clearly show that the SMBH strongly interacts with its environment, generating outflows/jets, bubbles, turbulence, and shocks that heat the surrounding hot atmosphere (e.g. McNamara & Nulsen 2007; Fabian 2012, for a review).

Multi-wavelength observations of massive ellipticals show nevertheless a multiphase ISM, suggesting that residual cooling occurs and regulates the triggering of the AGN and galaxy evolution. $H\alpha$ emission is regularly detected (e.g., Caon et al. 2000; McDonald et al. 2011; Sarzi et al. 2013; Werner et al. 2014) and probes photo-ionized warm $T \sim 10^4$ K gas (Haardt & Madau 2012). The warm gas typically occupies an irregular region several kpc in size and displays a complex and chaotic kinematics. Dust, associated with both the hot and cold ISM phases is also often detected (Temi et al. 2009; Smith et al. 2012; O’Sullivan et al. 2015). Recent observations have shown that [CII] emission is also a common presence in massive ellipticals (Werner et al. 2014). The [CII] and $H\alpha$ emitting gas are largely co-spatial, which suggests [CII] emission also traces the warm phase. While a significant fraction of the cold gas mass in low to intermediate mass early-type galaxies (ETGs) is thought to have an external, merger-related origin (e.g., Davis et al. 2011), in the most massive ETGs, of interest here, the cold and warm gas phases are likely generated by in-situ cooling (Davis et al. 2011; David et al. 2014; Werner et al. 2014).

Recent theoretical developments have shown that, while AGN-generated outflows and cavities globally inhibit cooling, they also stimulate residual cooling in spatially extended regions $\sim 1 - 10$ kpc in size, where the ratio of the cooling time to free-fall time is $t_{\text{cool}}/t_{\text{ff}} \lesssim 10 - 30$ (Revaz et al. 2008; Gaspari et al. 2011, 2017b; Sharma et al. 2012; Brighenti et al. 2015; Valentini & Brighenti 2015; Voit et al. 2015; Li et al. 2015; Barai et al. 2016; Lau et al. 2017).

The multiphase condensation mechanism might be related to the feeding of SMBHs, through the so-called chaotic cold accretion (CCA) mechanism (e.g., Gaspari et al. 2013, 2015, 2017b). In this scenario, warm filaments and cold clouds condense out of the hot halo, and recurrently boost the accretion rate up to a few orders of magnitude compared with hot (Bondi) accretion. The AGN responds by injecting back the energy in form of entrained massive outflows and/or relativistic jets, establishing a tight self-regulated loop (e.g., Gaspari & Sądowski 2017 for a brief review). During CCA the gas phases are spatially and kinematically correlated, showing comparable cooling and eddy turnover time $t_{\text{cool}}/t_{\text{eddy}} \approx 1$ (Gaspari et al. 2017a).

Currently, the coldest ISM phase (molecular or neutral gas) in normal massive elliptical galaxies is the least studied and not well characterized yet. Recent ALMA observations of the galaxy group NGC 5044 have revealed approximately 20 CO-emitting clouds in the central 10 kpc of the galaxy (David et al. 2014). In this paper we present new ALMA CO(2–1) observations of two group-centered elliptical galaxies (NGC 4636 and NGC 5846) to seek confirmation that molecular gas is a common presence in BGGs, and is not a result of merger events, but has cooled directly from the hot gas. In addition, we include a revised analysis of Cycle 0 ALMA observations of NGC 5044 that have been previously published by David et al. (2014). The current, more reliable pipeline, is used to reduce ALMA Cycle 0 data, known to suffer from early calibration issues. These three galaxies have the most complete observational coverage, with available deep *Chandra* X-ray data, SOAR and HST $H\alpha$ observa-

	NGC 5846	NGC 4636
AGN	yes	yes
AGN kinetic power (erg s ⁻¹)	7.5×10^{41}	3×10^{41}
$L_{H\alpha+[NII]}$ (erg s ⁻¹)	2.5×10^{40}	6×10^{39}
PAH lines (μm)	–	11.3, 17
Distance (Mpc)	24.2	17.1
ATLAS ^{3D} classification	slow-rotator	slow-rotator
effective radius (arcsec, kpc)	59, 6.9	89, 7.4
radio power (erg s ⁻¹)	2.5×10^{38}	1.5×10^{38}

Table 1

Summary of NGC 5846 and NGC 4636 properties, as measured or referenced in Allen et al. (2006); Caon et al. (2000); Trinchieri & Goudfrooij (2002); Werner et al. (2014); Rampazzo et al. (2013); Tonry et al. (2001); Mei et al. (2007); Emsellem et al. (2011); Cappellari et al. (2011); Cavagnolo et al. (2010).

tions, *Herschel* [CII] data, *Spitzer* FIR data and detailed HST dust absorption maps. All three galaxies satisfy the empirical criteria for extended multiphase gas cooling (Gaspari et al. 2013; Voit et al. 2015, 2017; Brighenti et al. 2015; Valentini & Brighenti 2015; Pulido et al. 2017, and references therein): central entropy $\lesssim 15$ keV cm² at radii of 5–15 kpc, minimum $t_{\text{cool}}/t_{\text{ff}} \lesssim 20$, $t_{\text{cool}} \lesssim 3 \times 10^8$ yr, and $t_{\text{cool}}/t_{\text{eddy}} \approx 1$. Equally important, they all exhibit X-ray evidence of recent feedback, bubbles, and radio emission, and each is expected to have low-entropy regions that are currently cooling (Gaspari et al. 2013; Voit et al. 2015, 2017; Brighenti et al. 2015; Valentini & Brighenti 2015).

2. GALAXIES SAMPLED

In this section we describe in depth the two galaxies for which new CO(2–1) data have been collected. We refer to David et al. (2014) for a description of NGC 5044. With the adopted distances of 31.2, 24.2, and 17.1 Mpc for NGC 5044, NGC 5846, and NGC 4636 (Tonry et al. 2001), the corresponding physical scales are 151, 118 and 83 pc per arcsec, respectively.

2.1. NGC 5846

NGC 5846, spherical in shape, is classified as a giant elliptical E0 and is the central and brightest galaxy in its group (Mahdavi et al. 2005).

Its proximity makes this object one of the closest example of AGN feedback in massive ellipticals. This is a very well studied system in every wavelengths other than at radio frequencies (Machacek et al. 2011). There is good knowledge of its hot ($\sim 10^7$ K) and ionized medium, while little is known about the content and the dynamics of the cold ($\leq 10^4$ K) phase, likely a significant component in the central kpc or so.

The dramatic effects of AGN outflows in NGC 5846 have been first discovered in the X-ray band, which probes hot ($\approx 10^7$ K) gas (Trinchieri & Goudfrooij 2002; Machacek et al. 2011). Two inner bubbles in the hot gas, at a distance of 600 pc from the center, filled with radio emission, are clear indication of recent AGN feedback. A weak radio source, elongated in the NE-SW direction, connects the inner cavities. X-ray bright rims surround the inner X-ray bubbles (Machacek et al. 2011). Many X-ray knots are visible, suggesting cooling sites. The scenario indicated by the *Chandra* observation is that of an AGN outflow, compressing and cooling the gas (e.g. Brighenti et al. 2015) in the central ~ 2 kpc ($20''$ at the distance of NGC 5846).

$H\alpha$ observations (Caon et al. 2000; Trinchieri & Goudfrooij 2002; Werner et al. 2014) reveal the presence of warm ($T \sim$

10^4 K) ionized gas in the inner 2 kpc of NGC 5846. Spectra of this gas indicate irregular motion, with typical velocity of 150 - 200 km s⁻¹. The warm 10^4 K gas traces the X-ray bright features, suggesting again a multiphase AGN outflow.

Using *Spitzer* IRS, Rampazzo et al. (2013) have detected mid infrared lines (e.g., [NeII] 12.81 μ m, [NeIII] 15.55 μ m), but no trace of polycyclic aromatic hydrocarbon (PAH) emission. Filho et al. (2004) have identified several sources in radio at 2.3, 5 and 15 GHz using VLBA data, these sources are aligned in the South-North direction.

Recent *Herschel* PACS observations have detected the presence of [CII] emitting gas that extends to a radius of ~ 2 kpc and is centrally peaked. The [CII] emission is almost exactly co-spatial with the of $H\alpha + [NII]$ emission and the total fluxes in [CII] and $H\alpha + [NII]$ have a ratio $F_{H\alpha+[NII]}/F_{[CII]} = 2.5$; a very similar flux ratio value observed in other group centered ellipticals (Werner et al. 2014). Furthermore, the velocities inferred from the [CII] line are consistent with those measured for the $H\alpha$ line (Caon et al. 2000). All these evidences suggest that the [CII] line is emitted by the warm gas, and it is not necessarily tracing the molecular phase.

NGC 5846 has another indication that the cold gas being disturbed by an AGN outburst. It has in fact an excess of cold ($T \sim 30$ K) dust, approximately co-spatial with the ionized and the molecular gas (Temi et al. 2007b; Mathews et al. 2013). With a 70 μ m luminosity of 3.5×10^{41} erg s⁻¹ (Temi et al. 2009), NGC 5846 shares the same dust properties of several giant ellipticals (e.g., NGC 4636 and NGC 5044; Temi et al. 2007a) which are best explained with ejection of dusty gas from their center by AGN activity that occurred $\sim 10^7$ yr ago. This dust has to still be embedded in cold gas, otherwise it would be sputtered away in $\sim 10^7$ yr.

2.2. NGC 4636

NGC 4636 is the central galaxy of a poor group in the outskirts of the Virgo Cluster. It harbors a relatively small SMBH of $7.9 \times 10^7 M_{\odot}$ (Merritt & Ferrarese 2001) as inferred from the bulge velocity dispersion.

The dramatic effects of AGN outflows in NGC 4636 have been first discovered in the X-ray band, which probes the hot ($\approx 10^7$ K) gas (Jones et al. 2002; Baldi et al. 2009). Large bubbles in the hot gas, surrounded by bright rims are likely the results of shocks generated by the AGN jets. A weak radio source, elongated in the NE-SW direction, connects the NE and SW bubbles.

Of major interest is the X-ray bright core, having a radius of ~ 1 kpc. As discussed in Baldi et al. (2009), the core shows a central cavity surrounded by a bright edge. Interestingly, the small X-ray cavity surrounds the ~ 1 kpc radio jet detected at 1.4 GHz (Allen et al. 2006), and is likely generated by the jet. Thus, the X-ray and radio observations point to a scenario in which gas may be currently outflowing in the central kpc of NGC 4636. UV emission (Bregman et al. 2001, 2005) exhibits O VI emission, which is a tracer of gas cooling. The measured emission indicates a cooling rate of $0.3 M_{\odot} \text{ yr}^{-1}$. Rampazzo et al. (2013) detected PAH emission at 11.3 and 17 μ m as well as [Ne II], [Ne III] and [S III] lines in the center of NGC 4636 (within $r_e/8$) using *Spitzer*-IRS. $H\alpha$ observations (Caon et al. 2000; Werner et al. 2014) reveal the presence of warm ($T \sim 10^4$ K) ionized gas in the inner kpc of NGC 4636. Spectra of this gas indicate irregular motion, with typical velocity of 150 - 200 km s⁻¹. $H\alpha$ maps of the galaxy core show the presence of a cavity in the distribution of the ionized gas,

encircled by a dense shell located at a distance of ~ 400 pc from the center. Again, the most plausible explanation is gas expansion caused by the AGN activity.

In NGC 4636 the [CII] emission extends to a radius of ~ 1 kpc and is centrally peaked. The velocities inferred from the [CII] line are consistent with those measured for the $H\alpha$ line. Finally, NGC 4636 has an excess of cold dust, approximately co-spatial with the ionized and the molecular gas (Temi et al. 2007a; Mathews et al. 2013). As above, this dust is expected to be embedded in cold gas, to be protected against rapid sputtering. In Temi et al. (2007a) we showed that the extended dust distribution originates from the ejection of cold gas by the AGN activity occurred 10 Myr ago.

3. OBSERVATIONS AND DATA REDUCTION

3.1. New Cycle 3-4 observations of NGC 5846 and NGC 4636

We observed NGC 5846 and NGC 4636 with ALMA during Cycle 3 (Project code: 2015.1.00860.S, PI: Temi). For both galaxies, the ALMA interferometer was configured such that its longest baseline was about 640 m and its shortest baseline about 15 m. This configuration resulted in an angular resolution of about $0.6''$ and a maximum recoverable scale of $5.4''$. Assuming a distance of 17.1 Mpc for NGC 4636 and 24.2 Mpc for NGC 5846, $0.6''$ and $5.4''$ correspond to 50 and 450 pc for NGC 4636 and 72 and 644 pc for NGC 5846, respectively. All data were taken in the ALMA band 6, one spectral window (spw) was centered around the CO (2-1) line and three other spws measured the continuum. A detailed description of the observations is presented in table 2.

The data were reduced using the CASA software (version 4.5.3 McMullin et al. 2007). As a first step we carefully checked the results of the quality assurance (QA) processes provided by the Science Pipeline team, focusing in particular on the calibration process. For NGC 5846, the pipeline calibration appears to be reasonable, therefore we simply produced the calibrated dataset by running the original pipeline reduction scripts. We further attempted the self-calibration, but the image quality did not improve. For NGC 4636, a bad antenna (DV02) partially corrupted the second execution block (EB), therefore we flagged it and performed a new manual calibration following the steps in the script provided to the PI, and then combined the two EBs to produce the final calibrated dataset. Self-calibration was attempted as well, but no good solutions were found.

The continuum-subtracted image cubes were produced using the CLEAN algorithm provided in the CASA package, and several velocity resolutions, Briggs weightings and threshold values were explored to determine the optimum setup for each image and to investigate the goodness of the detection. In the end, we used in this paper two thresholds to produce maps that will be used to detect the potential signals. One threshold corresponds to about 1.5 times the noise rms of the treated data, it is a more aggressive "cleaning" version. A lower threshold creates a lot of sources that most likely are just noise. The other threshold corresponds to about 4 times the noise rms of our data, it is a more conservative "cleaning". Using a much larger threshold would correspond to making a final image which is identical to the initial dirty map, since the signal-to-noise in our data is not very large and the algorithm would not find any signal to iterate on. Using thresholds between these two values does not produce significantly different results with our data, table 3 indicate with which threshold

	NGC 5846		NGC 4636	
Observation center (RA,DEC)	(15h 6m 29.253s, 1° 36' 20.290")		(12h 42m 49.867s, 2° 41' 16.010")	
	ALMA 12m			
Observation dates (yyyy/mm/dd)	2016/05/13		2016/05/02	2016/05/03
Observation duration (min)	71.15		49.21	48.81
On-target duration (min)	40.82		29.74	29.74
PWV (mm)	1.08		1.12	2.02
T _{sys} at 230 GHz (K)	75		74	90
Calibrators (flux, bandpass, phase)	J1517-2422, J1550+0527, J1505+0326		J1229+0203	
Line central wavelength (GHz)	229.23		229.83	
Line bandwidth & resolution (MHz, km s ⁻¹)	(937.5, 1200) & (0.5, 0.6)			
Continuum central wavelengths (GHz)	216.45, 218.17, 230.61		215.62, 217.33, 229.91	
Continuum bandwidth & resolution (MHz, km s ⁻¹)	(1850, 2400) & (31.25, 42)			
	ALMA Compact Array (ACA)			
Observation dates (yyyy/mm/dd)	2016/12/21	2017/04/29	2016/12/28	2017/03/26
Observation duration (min)	77.13	77.31	91.62	91.55
On-target duration (min)		34.27		49.90
T _{sys} at 230 GHz (K)	86	68	61	64
Calibrators (flux, bandpass, phase)	Callisto, J1256-0547, J1516+0015		J1256-0547, J1229+0203, J1229+0203	
Line central wavelength (GHz)	229.23		229.83	
Line bandwidth & resolution (MHz, km s ⁻¹)	(937.5, 1200) & (0.5, 0.6)			
Continuum central wavelengths (GHz)	214.02, 215.71, 228.02		214.33, 216.02, 228.52	
Continuum bandwidth & resolution (MHz, km s ⁻¹)	(1850, 2400) & (31.25, 42)			

Table 2
Summary of ALMA observations of NGC 5846 and NGC 4636

a source has been detected. CO maps in figures have been produced using the more aggressive threshold, since it returns a better S/N on maps.

In this paper, we present images and spectra obtained with 10 km s⁻¹ resolution image cubes and natural weighting (robustness parameter = 2), with the CLEAN algorithm running in non-interactive mode (threshold = 0.5 mJy, that roughly corresponds about 1.5 times the rms noise). This provided a synthesized beam of 0.79'' × 0.70'' with a position angle (P.A.) of 79° for NGC 5846 observations and a synthesized beam of 0.74'' × 0.67'' with a P.A. of 116° for NGC 4636. For the reasons explained above, the final images presented here are not self-calibrated. The rms noise in the line-free channels was 0.4 and 0.3 mJy beam⁻¹ for NGC 5846 and NGC 4636, respectively. Images of the continuum emission were also produced by averaging channels free of any line emission. An unresolved central continuum source is detected in both NGC 5846 and NGC 4636, with flux of 10.63 ± 0.03 mJy at 220.997 GHz and 0.4 ± 0.1 mJy at 221.390 GHz, respectively. The position of the continuum is in good agreement with radio and optical images with an offset of 0.10 ± 0.01 and 0.15 ± 0.01 arcsec for NGC 4636 and NGC 5846 respectively.

In addition to the ALMA 12-m array observations, we obtained complementary data from the ALMA Compact Array (ACA) for NGC 5846 and NGC 4636 in Cycle 4 (Project code: 2016.1.00843.S, PI: Temi). As for the 12-m observations, all data were taken in the ALMA band 6 with a similar spectral setup. These observations are presented in more details in table 2.

We used the products provided by the ALMA pipeline for ACA data. The pipeline used CASA 4.7.2 and CASA 4.7.38335 for NGC 5846 and NGC 4636, respectively. Using the Briggs weighting scheme with a robust parameter of 0.5, the resulting beam size was 7.0'' × 4.5'' and 6.8'' × 4.4'' for NGC 5846 and NGC 4636, respectively. The final estimates of the rms noise values are 4.02 and 2.45 mJy beam⁻¹ for NGC 5846 and NGC 4636 with a velocity bin of 10 km s⁻¹.

3.2. Re-analysis of Cycle 0 observations of NGC 5044

NGC 5044 was observed during Cycle 0 (Project code: 2011.0.00735.SSB, PI: Lim) and is described in details in David et al. (2014), we only summarize here the main characteristics of these observations. NGC 5044 was observed with an angular resolution of 2.0'' × 1.4'' for 29 minutes with a spectral resolution of 0.64 km s⁻¹ around the CO(2-1) emission line.

Given the uncertainties associated with the early phase of ALMA data reduction and calibration, we decided to reduce again the NGC 5044 observations with the latest release of the CASA reduction and calibration software package. In particular, we followed the CASA guides⁹ to modify the packaged calibration script in order to apply the proper amplitude calibration scale (which has changed since Cycle 0) and also remove some atmospheric lines in the calibrators. The channel containing these lines were further removed from the calibrated target in order to perform a correct continuum subtraction.

Similarly to what was done for NGC 5846 and NGC 4636, we present here the images and spectra obtained with 10 km s⁻¹ resolution image cubes and natural weighting, with the CLEAN algorithm running in non-interactive mode (threshold = 1.6 mJy, that roughly corresponds to 1.5 time the rms noise). This provided a synthesized beam of 1.99'' × 1.41'' with a position angle (P.A.) of 148°. The rms noise in the line-free channels was 1.0 mJy beam⁻¹.

4. RESULTS

Using Cycle 0 ALMA observations, David et al. (2014) discovered over 20 CO(2-1) emitting clouds in the brightest X-ray galaxy/group NGC 5044. With our new ALMA Cycle 3 observations, we seek confirmation that CO molecular clouds

⁹ https://casaguides.nrao.edu/index.php/Guide_To_Reddo_Calibration_For_ALMA_Cycle_0; https://casaguides.nrao.edu/index.php/Updating_a_script_to_work_with_CASA_4.2

ID	(RA,DEC) offset ($''$),(kpc)	$\langle v \rangle$ (km s $^{-1}$)	σ (km s $^{-1}$)	$S_{CO}\Delta v$ (Jy km s $^{-1}$)	M_{mol} ($10^5 M_{\odot}$)	Ang. Size FWHM ($''$)	Phys. Size (pc)	Methods
NGC 5846								
1	(-2.3,-1.5),(-0.3,-0.2)	-230.7 ± 1.6	23.3 ± 1.6	0.32 ± 0.02	6.4 ± 0.4	1.2 ± 0.2 $\times 0.2 \pm 0.2$	143×24	I,F,i,f
2	(-0.8,-18.0),(-0.1,-2.1)	-155.4 ± 3.0	14.6 ± 3.0	0.24 ± 0.04	4.8 ± 0.8	< 0.7	< 82	i,f
3	(8.2,3.2),(1.0,0.4)	110.6 ± 1.6	19.9 ± 1.6	0.45 ± 0.04	8.9 ± 0.7	2.9 ± 0.3 $\times 0.7 \pm 0.04^{\dagger}$	346×83	I,F,i,f
NGC 4636								
1	(-19.0,-0.3),(-1.6,-0.0)	140.3 ± 8.4	26.4 ± 8.4	0.20 ± 0.06	1.9 ± 0.5	< 0.7	< 50	i,f
2	(2.0,0.3),(0.2,0.0)	209.5 ± 3.9	25.8 ± 3.9	0.07 ± 0.01	0.7 ± 0.1	< 0.7	< 50	I,F,i,f
NGC 5044								
1	(-0.1,-2.0),(-0.0,-0.3)	-556.9 ± 11.9	67.0 ± 10.7	0.8 ± 0.1	24.4 ± 3.8	< 2.0	< 300	I,F,i,f
2	(0.0,2.8),(0.0,0.4)	-313.1 ± 9.5	36.6 ± 9.4	0.4 ± 0.1	12.2 ± 2.5	< 2.0	< 300	I,F,i,f
3	(-2.2,-1.4),(-0.3,-0.2)	-274.4 ± 4.5	28.4 ± 4.4	0.4 ± 0.1	12.8 ± 1.8	< 2.0	< 300	F,i,f
5	(-12.0,-5.2),(-1.8,-0.8)	-192.8 ± 6.6	30.5 ± 8.5	0.7 ± 0.1	23.2 ± 3.8	< 2.0	< 300	F,i,f
6	(-1.9,1.8),(-0.3,0.3)	-226.8 ± 4.3	20.4 ± 4.3	0.3 ± 0.1	9.5 ± 1.8	< 2.0	< 300	I,F,i,f
7	(-1.3,6.4),(-0.2,1.0)	-207.0 ± 6.9	31.1 ± 6.4	0.4 ± 0.1	12.6 ± 2.5	< 2.0	< 300	F,i,f
8	(-0.4,-0.4),(-0.1,-0.1)	-148.8 ± 8.2	76.2 ± 7.2	1.1 ± 0.1	33.9 ± 3.1	3.9 ± 1.3 $\times 1.2 \pm 0.6$	590×182	I,F,i,f
11	(3.0,-2.6),(0.5,-0.4)	-95.8 ± 6.0	41.0 ± 4.9	0.5 ± 0.1	16.5 ± 2.4	< 2.0	< 300	F,i,f
12	(-8.6,3.4),(-1.3,0.5)	-132.9 ± 3.9	18.4 ± 3.9	0.4 ± 0.1	13.6 ± 2.5	< 2.0	< 300	F,i,f
13	(-1.2,-2.4),(-0.2,-0.4)	-80.9 ± 6.9	43.1 ± 8.1	0.8 ± 0.1	26.0 ± 2.6	3.8 ± 1.0 $\times 0.7 \pm 0.7$	575×106	I,F,i,f
14	(-14.4,-5.8),(-2.2,-0.9)	-46.8 ± 10.6	39.0 ± 8.2	1.0 ± 0.2	30.7 ± 7.2	3.1 ± 1.3 $\times 1.0 \pm 0.6$	469×151	F,i,f
18	(0.8,1.2),(0.1,0.2)	27.8 ± 1.7	37.4 ± 1.7	3.0 ± 0.1	93.8 ± 3.7	1.9 ± 0.2 $\times 0.8 \pm 0.5$	287×121	I,F,i,f
20	(-15.0,-7.8),(-2.3,-1.2)	29.2 ± 12.8	73.0 ± 12.8	1.2 ± 0.2	37.6 ± 6.0	< 2.0	< 300	F,i,f
21	(-8.4,11.0),(-1.3,1.7)	41.8 ± 9.3	46.8 ± 8.4	1.0 ± 0.2	32.0 ± 5.5	< 2.0	< 300	F,i,f
22	(1.2,14.4),(0.2,2.2)	-18.3 ± 26.1	125.6 ± 24.6	1.7 ± 0.3	53.2 ± 9.0	< 2.0	< 300	F,i,f
25	(17.3,10.4),(2.6,1.6)	-573.7 ± 3.2	10.3 ± 2.1	0.7 ± 0.2	22.8 ± 6.6	< 2.0	< 300	i,f
26	(15.8,-12.8),(2.4,-1.9)	-108.1 ± 3.3	10.9 ± 3.4	0.6 ± 0.2	19.2 ± 5.4	< 2.0	< 300	i,f

Table 3

Cloud candidates for NGC 5846 (top), NGC 4636 (center) and NGC 5044 (bottom) with their location with respect to the galaxy center (offset along RA,DEC axis in arcsec and kpc), their average velocity, their velocity dispersion, their total CO(2-1) flux (corrected from the primary beam effect), the corresponding molecular mass calculated using Eq. 1, the dimension of the cloud (in arcsec and pc) and the methods with which the clump was detected (i when detected in the image, f when detected in the spectrum with a 1.5 noise rms cleaning threshold, I and F when detected with a 4 noise rms cleaning threshold). To be consistent with cloud labeling in David et al. (2014), the original cloud number sequence for NGC 5044 has been maintained. The spectral properties have been calculated with a Gaussian fitted on the sum of the emission from pixels with a signal-to-noise larger than 4. The dimension of the cloud were calculated with the *imfit* function of CASA and correspond to the deconvolved FWHM † : for cloud #3 of NGC 5846, the dimension of the cloud is not deconvolved from the beam, given the minor axis length is too close to the beam size.

are common features in group-centered elliptical galaxies that are, in many respects, similar to NGC 5044.

In order to identify CO clouds in our data, we used the cubes described previously and 3 other sets of cubes for each galaxy. One set was produced by increasing the threshold of the cleaning algorithm to 1.5 mJy for NGC 5846 and NGC 4636 and to 4 mJy for NGC 5044 (roughly 4 times the rms noise) from 0.5 and 1.6 mJy. Two extra sets were produced by refining the velocity resolution to 3 km s $^{-1}$ and setting the CLEAN threshold to 0.9 and 2.5 mJy for NGC 5846 and NGC 4636, and to 1.6 and 7 mJy for NGC 5044, respectively (thresholds were scaled with the bin size, $\sqrt{10/3}$). This thinner spectral resolution is needed to perform the detection of the lines in the spectral domain. Our detection technique requires to convolve the signal by a Gaussian kernel as thin as 9 km s $^{-1}$ wide and the 3 km s $^{-1}$ provides an adequate sampling to do so.

With each 10 km s $^{-1}$ cubes (2 per galaxy), we identified clouds in each images by detecting pixels with a flux larger than five times the rms noise. These sets of pixel-channel are then clustered together (spatially and between velocity channels)

to form a list of cloud candidates.

With each 3 km s $^{-1}$ cubes (2 per galaxy), we whitened the noise by multiplying each pixel frequency stream by a function in Fourier mode that approximates well the noise power spectrum of these time streams; this operation reduces the effect of the Hanning filter introduced by the ALMA processing. We then convolved each pixel spectra by Gaussian kernels of various width ($\sigma = 9, 18, 30, 45, 60$ km s $^{-1}$) and selected pixels with signal larger than 5 times the rms noise. Again, we clustered these lists of pixel-velocity to obtain a list of cloud candidates. Both of these techniques are tuned to measure lines larger than about 10 km s $^{-1}$ given one is using a 10 km s $^{-1}$ bin size and the other has a smallest kernel of 9 km s $^{-1}$. Using thinner spectral resolution is very challenging with the data collected that do not have a large signal-to-noise ratio. Furthermore, given the angular resolution of these observations it is not expected that we could resolve individual GMCs with small velocity dispersion but more likely some GMAs with a typical velocity dispersion of a few tenths of km s $^{-1}$.

We produced a combined list of cloud candidates from these

4 clouds candidate lists by requiring at least 1 detection in the image and 1 detection in the spectrum. The final list of cloud candidates presented in this paper (Table 3) was obtained by requiring that each cloud line had a minimal velocity dispersion of 6 km s^{-1} and a total signal-to-noise ratio of 6. We increased the signal-to-noise ratio criteria to 6 in order to remove potential false detections, given the data sample size is of a few millions (depending on the velocity resolution). A signal-to-noise of 5 could still return a few false detections (1 per 3 million sample on average). We note however that the velocity dispersion criteria and the requirement to detect the line in a pixel spectrum as well as in the image is more stringent and that a signal-to-noise of 5 return the same cloud candidate for our data. The minimum velocity dispersion of 6 km s^{-1} allows to sample properly the lines, given the data have been analyzed at velocity resolution of at most 3 km s^{-1} .

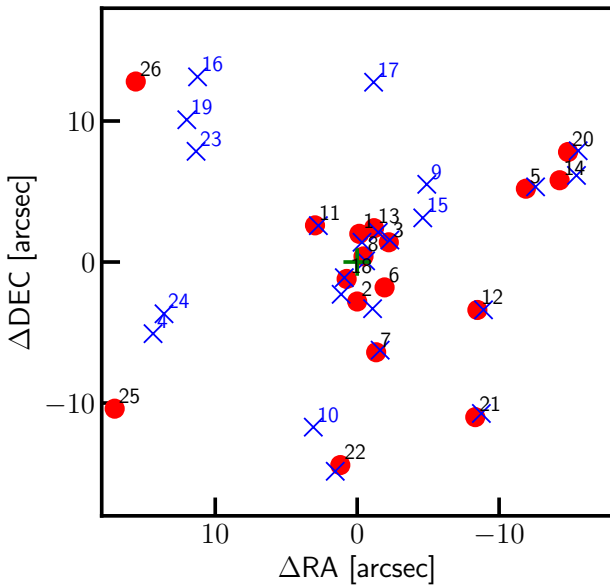


Figure 1. CO clouds detected in NGC 5044. Blue crosses and red dots show the location of CO clouds detected by David et al. (2014) and with our updated reduction, respectively. For consistency with cloud labeling in David et al. (2014), the original cloud number sequence has been maintained. Our detection criteria did not confirm 9 clouds previously listed by David et al. (2014), while two new clouds, 25 and 26, are now apparent in the field.

The rather conservative approach used in selecting cloud candidates makes us worry about losing real clouds that could have been marginally detected. Indeed, by relaxing the selection criteria to a signal-to-noise ratio greater than 3 and allowing a detection in either the spatial or velocity space, a number of cloud candidates become apparent in NGC 5846 and NGC 4636. These additional clouds seem to follow closely the filaments and ridges evident in the $\text{H}\alpha$ + $[\text{NII}]$ image, and are not randomly distributed in the field as expected from spurious signals. Although there are hints that these clouds may be real with a low-level detection, we decided not to include them in our analysis because often their extent in the velocity domain was very limited and the detection was not confirmed in the spatial plane. Deeper ALMA observations would be required to confirm a positive detection of these clouds.

The final list of clouds contains 3 detections for NGC 5846, 2 for NGC 4636 and 17 for NGC 5044. Our new data reduction and cloud selection criteria for NGC 5044 yield a lower

number of clouds detection (17) when compared to the earlier published list (24) by David et al. (2014). Figure 1 shows the location of CO clouds detected by David et al. (2014) and with our updated reduction as blue crosses and red dots, respectively. To be consistent with cloud labeling in David et al. (2014), the original cloud number sequence has been maintained. There are 9 unconfirmed clouds previously listed in David et al. (2014), and two new clouds, 25 and 26, that passed our detection criteria. The vast majority of clouds in the central region are confirmed as well as is the ridge of clouds extending to the north-west part of the sky. The reason for the discrepancy in CO cloud detection in NGC 5044, may be caused by the selection criteria that we used to detect clouds. Indeed, David et al. (2014) used a lower signal-to-noise ratio of 4 as threshold for cloud detection in the earlier NGC 5044 reduction. To avoid false-positive detections we set our criteria to be quite restrictive and conservative, requiring a robust signal-to-noise ratio threshold to be met. This is supported by the fact that most of the missing clouds resides toward the edge of the primary beam extension where the instrumental noise is higher. Also, some of the confirmed clouds are displaced by $\sim 1''$ when compared with the cloud location of our new reduction. This may be due to updated housekeeping astrometry in the CASA software. The physical properties of the confirmed clouds in NGC 5044 will be discussed in the following sections, but in general terms they are in good agreement with results previously published by David et al. (2014).

4.1. CO Clouds in NGC 5846 and NGC 4636

Figure 2 and Figure 3 show the distribution of the CO(2-1) detected clouds in NGC 5846 and NGC 4636 projected against an $\text{H}\alpha$ + $[\text{NII}]$ map (left panel) and a HST dust absorption map (right panel). The $\text{H}\alpha$ + $[\text{NII}]$ images have been taken with the SOAR telescope with an average seeing of $\sim 0.7''$. The registration of the $\text{H}\alpha$ + $[\text{NII}]$ and CO images is correct within an uncertainty of about $0.2''$ due to the astrometry in the SOAR data (Werner et al. 2014). In the figures, the optical dust maps were generated from archival HST data recorded with the WFPC2 in the F555W, F547M and F814W filters.

Two of the three CO clouds detected in NGC 5846, cloud #1 and #3 are resolved in at least one direction by the 12 meter array observations and extend to $1.2''$ and $2.9''$, respectively. Black and white contours outline CO clouds, and are defined as the area where the emission line signal-to-noise is greater than 4. Cloud #2 in NGC 5846 and #1 in NGC 4636 are outside the field of view of the high resolution HST dust map. These clouds are also quite close to the edge of the ALMA primary beam and were only detected when the cleaning threshold was set to about 1.5 times the rms noise, therefore they could still be artefacts created by the “cleaning” algorithm.

Three out of five clouds detected in these two galaxies are located in a region where the $\text{H}\alpha$ + $[\text{NII}]$ emission is relatively large although not in the strongest emission region and not quite at the center of the galaxy. Clouds #1 and #3 in NGC 5846 are about $5.5''$ and $8.4''$ away (0.6 and 1.0 kpc) from the galaxy center and cloud #2 in NGC 4636 is about $2.6''$ away from the central nucleus (200 pc).

The HST images have a $25''$ field of view and only central cloud contours are visible. There is a good correlation between the cloud position and the dust absorption in both NGC 5846 and NGC 4636, although several heavily obscured parts of each galaxies do not show CO(2-1) surface brightness large enough to be detected in our data.

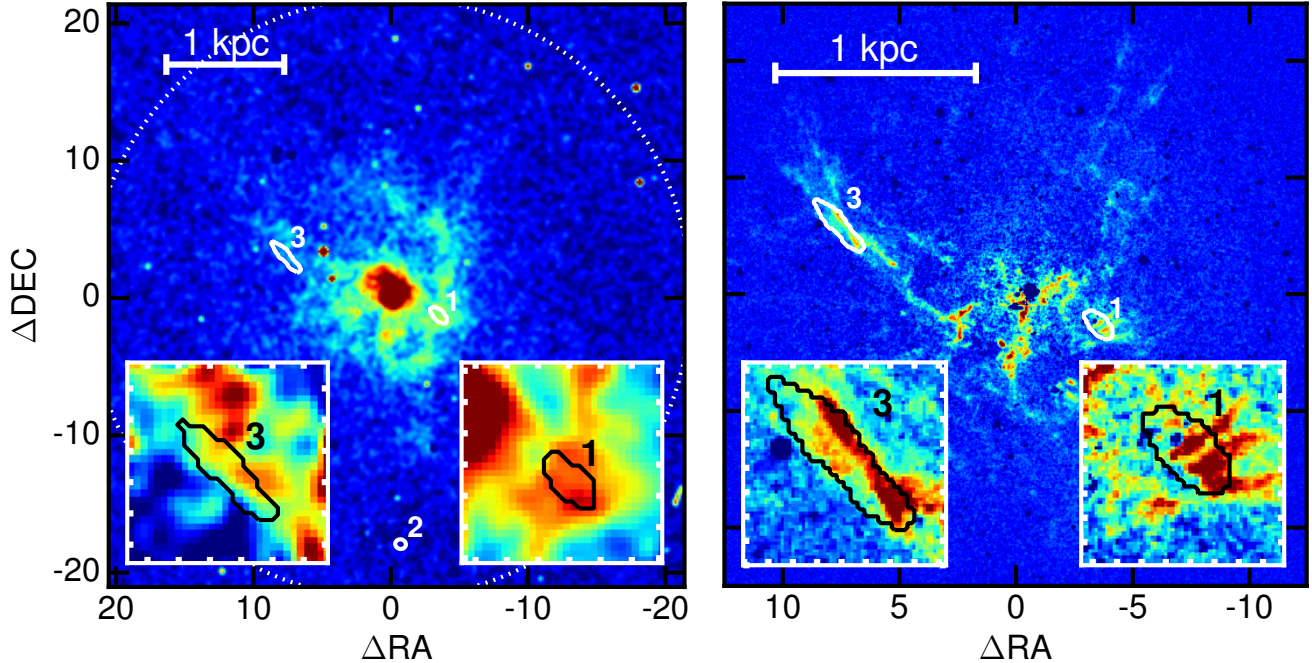


Figure 2. Images of NGC 5846 showing detected CO(2-1) clouds projected against an optical $H\alpha+N[II]$ emission (left) and a dust starlight extinction image (right). Color sequence (blue \rightarrow green \rightarrow yellow \rightarrow red) indicates increasing $H\alpha+N[II]$ and dust. CO clouds, indicated with black (in the insert) and white contours, are defined as the area where the emission line signal-to-noise is greater than 4. Clouds #1 and #3 are somewhat resolved and extend about $1.2''$ and $2.9''$. Note that cloud #3 (see enlarged insert) is aligned almost exactly along a dust filament, and coincides with knots and filamentary structures in the $H\alpha+N[II]$ emission. Cloud #1 also coincides with $H\alpha+N[II]$ emission and dust extinction, but other similar dusty regions were not detected in CO(2-1). Cloud #2 is not associated with detectable optical emission and out of dust extinction map FOV. The registration of the $H\alpha+N[II]$ and CO images is correct within an uncertainty of about $0.1''$ – $0.2''$ in the astrometry in the SOAR data. The effective radius of NGC 5846 in the K-band is $35.75''$. The white dashed circle in the $H\alpha+N[II]$ emission map identifies the field of view of the ALMA primary beam.

In NGC 5846, cloud #3 is aligned almost exactly along a dust filament, while cloud #1 also coincides with small dust extinction structures (about $0.5'' \sim 60$ pc wide), but other similar dusty regions were not detected in CO(2-1). Cloud #2 in NGC 4636 is located in the same area of one of the most obscured region of NGC 4636. Both clouds in NGC 4636 are not resolved by these observations, implying an angular size $\leq 0.7''$ (~ 50 pc).

Figure 4 show the spectra of the five CO(2-1) clouds detected. For the two resolved clouds (clouds #1 & #3 in NGC 5846), the spectra have been obtained by summing the signal from the pixels of each cloud (contiguous pixels with a signal-to-noise ratio greater than 3 times the rms noise within the velocity range of the emission line). For unresolved clouds, the spectra is taken from the pixels with the largest signal-to-noise within the velocity range of the emission line.

A Gaussian fit to the emission line is presented as a red line in Figure 4. Cloud #1 in NGC 4636 has a double peaked spectrum that cannot be fitted with a single gaussian curve. The spectrum could be interpreted as generated by two distinct clouds that have similar projected position on the sky, but with a differential peak-to-peak velocity of ~ 40 km s^{-1} . Unfortunately, since the cloud is not resolved by our current ALMA configuration, we cannot quantify its kinematics properties, including its gas velocity dispersion.

4.2. CO Clouds in NGC 5044

Our new reduction of the Cycle 0 ALMA data on NGC 5044 confirmed the detection of 17 CO(2-1) clouds. Figure 5 shows the distribution of the detected clouds overlapped to a false color $H\alpha+N[II]$ map (left panel) and a HST dust absorption map (right panel). Most of the clouds in NGC 5044 are lo-

cated within a radius of approximately $5''$ around the center of the galaxy. In Figure 5, unresolved clouds are identified with an ellipse roughly the size of the beam, while contours, at 4 times the rms noise level, are used to represent the extended molecular clouds/associations. With a resolution of $2.0'' \times 1.4''$, only four clouds are resolved by these observations: cloud #8, #13, #14 and #18.

The HST dust extinction map presents several compact knotty features in its central region. All of the central CO clouds lie on top of these strong dust absorption features, with the larger (resolved) clouds encompassing few clumps of dust. In the central $5'' \times 5''$ there is a good correlation between dust features and molecular cloud. However, more distant clouds in HST field of view (clouds #7, #12, #21) are not correlated with dust absorptions.

The $H\alpha+N[II]$ emission map shows a very peaked central emission with the addition of diffuse and filamentary structures that extend up $30''$ from the galaxy center. From the total of 17 clouds, 12 are located where the $H\alpha+N[II]$ emission is fairly large and 8 of these clouds are within $4.6''$ from the center of the galaxy. In this central $\sim 5''$ region, the molecular clouds are located where the $H\alpha+N[II]$ emission is strongest, broadly providing a correlation between optical line emission and CO gas. On the other hand, the spatial distribution of the 8 central clouds does not rigorously follow the morphology of the $H\alpha+N[II]$ emission (see insert in Figure 5). Given the weak angular resolution of NGC 5044 CO(2-1) observation, we cannot exclude that some better correlation exists with a subset of clouds. The remaining 5 clouds (#5, #14, #20, #25, #26) are located far from the center, between $12''$ to $22''$. Clouds #25 & #26 were only detected with the cleaning threshold set to 1.5 times the rms noise, they could be artifacts

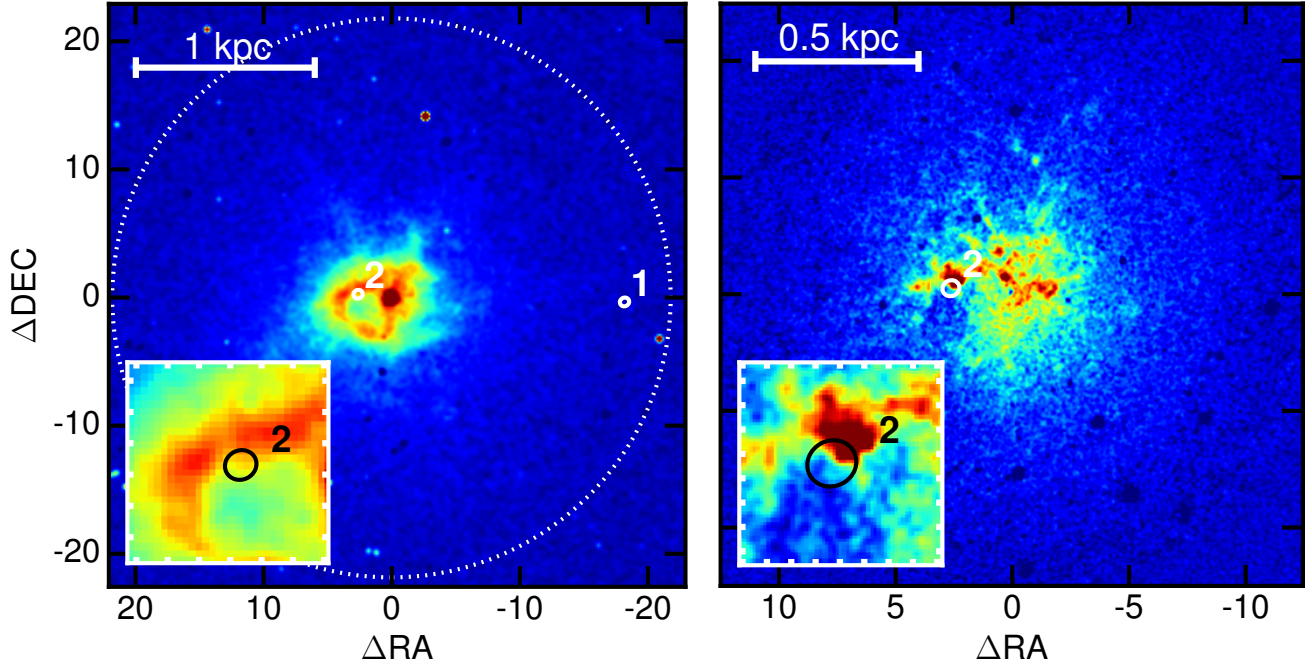


Figure 3. CO(2-1) clouds in NGC 4636 projected against the galaxy images (same as in Figure 2). Cloud #1 is not associated with detectable optical emission and out of the dust extinction map FOV, while cloud #2 is centered on a dust absorption knot and also aligned with a ridge in the optical line emission map. None of the clouds in NGC 4636 are resolved. The effective radius of NGC 4636 in the K-band is $56.29''$. The white dashed circle in the $H\alpha+N[II]$ emission map identifies the field of view of the ALMA primary beam.

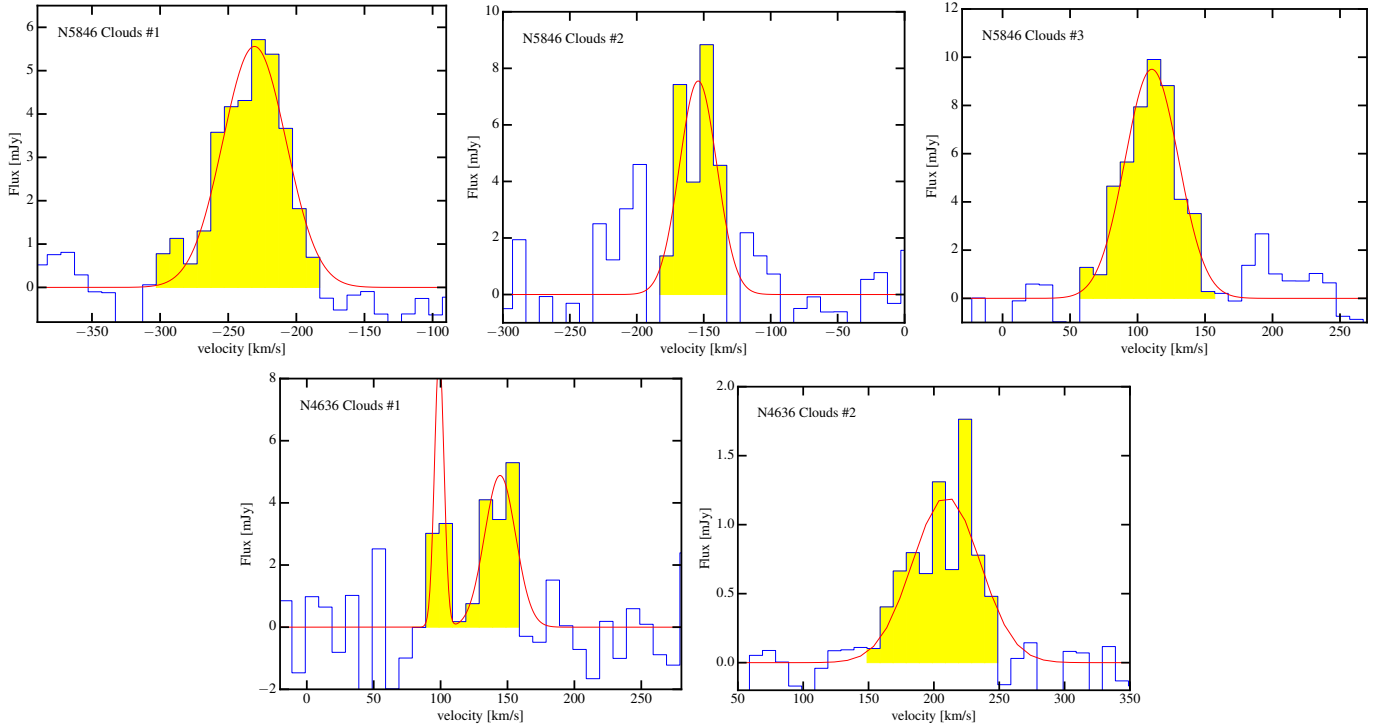


Figure 4. Spectra of the 5 clouds detected in ALMA CO(2-1) images of NGC 5846 (top) and NGC 4636 (bottom), with a Gaussian fit to the emission line (red). Cloud #1 and #3 spectra of NGC 5846 were computed respectively over 144 and 221 pixels covering a solid angle of 1.4 and 2.2 arcsec² (contiguous pixels with signal-to-noise ratio greater than 3), whereas since the other clouds are unresolved, the spectra correspond to the pixel with the largest signal-to-noise.

created by the “cleaning” algorithm.

Figure 6 show the spectra of the 17 CO(2-1) clouds detected. For the four resolved clouds, the spectra have been obtained using a similar procedure described earlier for NGC 5846. Also, for unresolved clouds, the spectra is taken

from the pixels with the largest signal-to-noise within the velocity range of the emission line. A Gaussian fit to the emission line is presented as a red line in Figure 6. The spectra are displayed with a bin size in velocity of 10 km s^{-1} . Since cloud

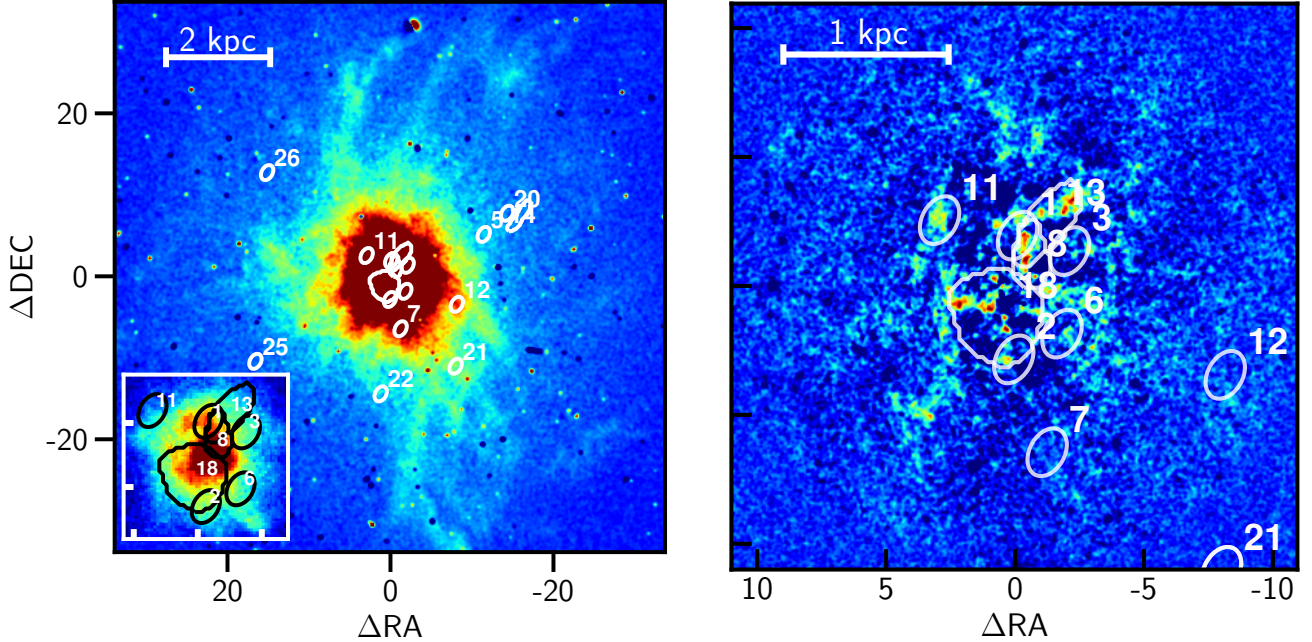


Figure 5. Images of NGC 5044 showing detected CO(2-1) clouds projected against an optical $H\alpha+N[III]$ emission (left) and a dust starlight extinction image (right). Color scheme of the background images and the cloud contours are as described in 2). The revised data reduction accounts for 17 CO clouds in the central ~ 6 kpc). Cloud labeling reflects the original sequence presented in David et al. (2014). The combination of newer pipeline software and a more stringent set of criteria for clouds detection did not confirm few CO clouds originally listed in David et al. (2014). Clouds #8, #13, #14, and #18 are resolved. Three of the four resolved clouds reside in the ~ 2 kpc (see enlarged insert) and overlap with several knot in the dust extinction maps as well as with the $H\alpha+[NII]$ emission in the galaxy center. The registration of the $H\alpha+[NII]$ and CO images is correct within an uncertainty of about $0.1'' - 0.2''$ in the astrometry in the SOAR data.

#22 has a large velocity dispersion, its spectrum is presented with a velocity bin size of 50 km s^{-1} .

5. ANALYSIS

Table 1 contains the basic parameters of the detected clouds, including the average velocity, their velocity dispersion, and total flux (corrected from the primary beam effect), as well as, the corresponding molecular mass and cloud dimension. The velocity and velocity dispersion has been obtained by fitting a Gaussian on the spectra of each clouds. For each cloud, the flux has been obtained by summing the emission of the spectra described previously and range from 70 to $3000 \text{ mJy km s}^{-1}$. The molecular mass of each cloud is computed by using (Bolatto et al. 2013)

$$M_{mol} = 1.05 \times 10^4 \left(\frac{X_{CO}}{2 \times 10^{20}} \right) \frac{S_{CO} \Delta \nu D_L^2}{(1+z)} M_{\odot}, \quad (1)$$

where $S_{CO} \Delta \nu$ is the integrated line flux density in Jy km s^{-1} in the ground rotational transition $J = 1 \rightarrow 0$, D_L is the luminosity distance to the source in Mpc, and z is the redshift. Throughout the paper we use the *reference* conversion factor $X_{CO} = 2 \times 10^{20} \text{ cm}^{-2} (\text{K km s}^{-1})^{-1}$ to evaluate the molecular gas mass in each detected cloud.

To convert the CO(2-1) flux into CO(1-0) flux, we assume that the CO(2-1) to CO(1-0) temperature brightness ratio is 0.8 as found by Braine & Combes (1992) so that the flux density ratio is 3.2 due to the frequency factor (David et al. 2014). The ACA data do not exhibit any detection and the clouds detected in the 12m array data are below the sensitivity of the ACA data. Cloud #3 of NGC 5846 has a peak flux density of 10 mJy in a 10 km s^{-1} bin that only represents a 2.5 rms noise signal at the center of the ACA observation. Cloud #1

of NGC 4636 has a peak flux density of about 5.5 mJy in 10 km s^{-1} bin that only represents a 2.3 rms noise signal at the center of the ACA observation. Using the known location in space and in velocity of cloud #3 of NGC 5846, we measure a signal with a flux density of $8.1 \pm 2.0 \text{ mJy/beam}$ by increasing the bin size to 50 km s^{-1} . However we detect other sources as well. Given the large amount of data, we expect several spurious detections at 4 time the rms noise. We verify that ACA data are consistent with the 12m data, but the ACA data alone are not sufficient to detect even cloud #3 of NGC 5846.

Using the reference X_{CO} factor, the derived molecular masses of the detected clouds vary from 1×10^5 to $9 \times 10^6 M_{\odot}$. For clouds that have been resolved along at least one of their dimension by ALMA observations, we used the *imfit* function from the CASA package to calculate their size. For simplicity, we refer to these clouds as resolved or extended even if one of their dimension is smaller than the beam. *imfit* fits an elliptical Gaussian component and returns the size of the major/minor axis and of the position angle, as well as their associated errors (Condon 1997). This model might not be the best match for the molecular cloud shape, however our measured residuals are consistent with pure noise, which might be due to the fact that none of the clouds is very well resolved. The values quoted in Table 3 correspond to the size deconvolved from the beam, except for cloud #3 of NGC 5846, because its fitted minor axis is too close to the beam size (within the beam size considering the uncertainties), so the size of the minor axis can not be deconvolved.

Clouds #1 and #3 in NGC 5846 measure $1.2''$ and $2.9''$ (major axis) respectively; these scales correspond to a physical size of 143 and 346 pc. Clouds #8, 13, 14, 18 measure $3.9''$, $3.8''$, $3.1''$ and $1.9''$ (major axis) corresponding to 590, 575, 469 and 287 pc. It is not clear whether these clouds are really

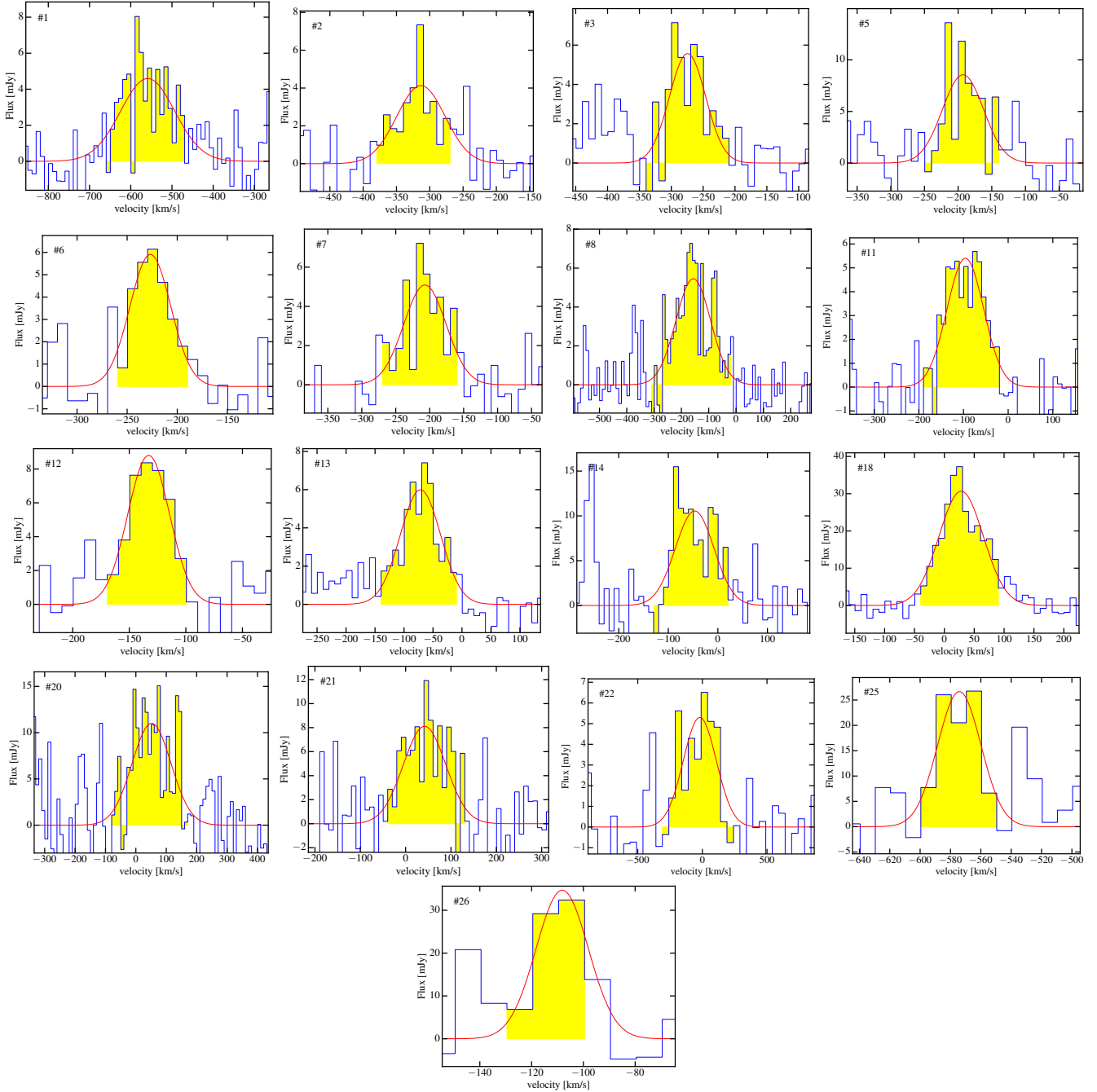


Figure 6. CO(2-1) spectra of the 17 clouds detected in NGC 5044 along with a Gaussian fit to the emission line (red curve). The velocity bin size is 10 km s^{-1} except for the cloud #22 where the bin size is 50 km s^{-1} .

contiguous or formed of several smaller clouds. Unresolved clouds are constrained to have a physical size smaller than 82, 50 and 300 pc for NGC 5846, NGC 4636 and NGC 5044 respectively given the angular resolution of our ALMA observations and the assumed distance of these galaxies.

The larger surface brightness and size of clouds #1 and #3 in NGC 5846 and clouds #8, 13, 14 and 18 in NGC 5044 allow to map out their properties. Figures 7 & 8 present the surface brightness, velocity and velocity dispersion maps of NGC 5846 & NGC 5044 clouds. The surface brightness has been calculated by integrating between -3σ and $+3\sigma$ (the velocity dispersion σ is fitted on the spectra) the spectra of each pixel (-303 to -163 km s^{-1} and 37 to 157 km s^{-1} for cloud #1

& #3 of NGC 5846 for instance). The velocity and velocity dispersion have been calculated by fitting a Gaussian to each pixel spectrum. The elongation and potential bimodality of the surface brightness of cloud #3 of NGC 5846 could indicate that it might be composed of 2 nearby (in projection) clouds. The velocity vary slowly along the major axis of the cloud from about 100 km s^{-1} to 120 km s^{-1} and could either substantiate the existence of 2 clouds or indicate some rotation of a larger cloud. The velocity dispersion of cloud #3 is fairly uniform between 17 and 21 km s^{-1} , given the uncertainty of about 5 km s^{-1} , and only seems to increase to 25 km s^{-1} at the edges of the major axis. Our observation angular resolution is not quite good enough to distinguish a two or one cloud

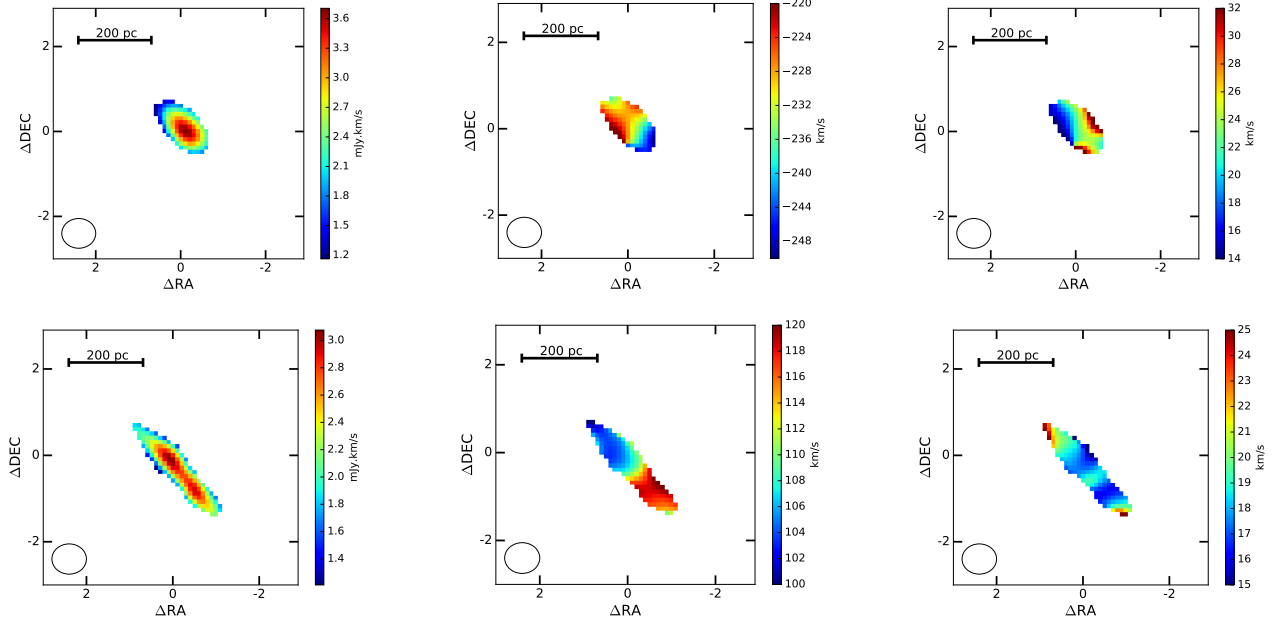


Figure 7. Flux (left), velocity (center) and velocity dispersion (right) in cloud #1 (top) and #3 (bottom) of NGC 5846. The flux image has been calculated by integrating the signal from -303 to -163 km s^{-1} and 37 to 157 km s^{-1} respectively, flux errors are typically about 0.3 mJy km s^{-1} . Velocity and velocity dispersion have been obtained by fitting the emission line and have a typical respective uncertainty of 4 and 5 km s^{-1} . The ellipse in the left bottom corner represents ALMA beam size.

scenario.

Cloud #1 of NGC 5846 has a more unimodal surface brightness shape and its surface brightness peaks roughly at its center. The velocity is varying across the cloud with a $\Delta v = 25$ km s^{-1} , which given the uncertainty of 4 km s^{-1} , is statistically significant. The shape of the velocity distribution is compatible with tidal disruption. The velocity dispersion vary quite significantly within the cloud, from 15 km s^{-1} to 32 km s^{-1} (error estimate is about 4 km s^{-1}).

All resolved clouds of NGC 5044 are quite unimodal and all clouds but cloud #15 are fairly elongated. They have a much larger velocity spread along their major axis ($\Delta v \sim 60$ to 80 km s^{-1}) compared to resolved clouds in NGC 5846 ($\Delta v \sim 20$ to 30 km s^{-1}).

5.1. Continuum

All three galaxies analyzed in this paper have a detected continuum around the CO(2-1) line. The measured continuum for NGC 4636, NGC 5846, NGC 5044 is respectively 0.4 ± 0.1 , 10.63 ± 0.03 , and 52.8 ± 1.5 mJy . Each continuum is detected as a point source with a size limited by the PSF of the observation (about $0.6''$ for NGC 4636 and NGC 5846 and $1.7''$ for NGC 5044, corresponding to 51 and 255 pc).

An absorption feature seen in the NGC 5044 continuum spectrum of the central continuum source shows that the emission must be very compact and probably arises from the AGN (David et al. 2014). We have not detected any absorption feature associated with the central continuum source in NGC 5846 or NGC 4636

Using FIR data from *Spitzer* and *Herschel*, when available, as well as radio data, it is possible to fit for the FIR and radio spectra to weight the contribution of each to the continuum at 230 GHz as seen by ALMA. FIR data from *Spitzer* and *Herschel* were taken from Temi et al. (2009) and Amblard et al. (2014) respectively, in these data all three galaxies are unresolved. The radio data were taken from a variety

of observations Vollmer et al. (2004); Nagar et al. (2005); Filho et al. (2004); Giacintucci et al. (2011), the fluxes were corrected assuming uniform brightness when the scale at which they were measured differed greatly from ALMA PSF.

Figure 9 summarizes observations between 10 μm (30 THz) and 1 m (300 MHz) for our three galaxies. NGC 4636 has the best coverage in the FIR with data from *Herschel*-SPIRE. The fit of a FIR modified black body spectra (emissivity $\beta=1.5$) returns a temperature of 31.8 ± 0.9 , 30.0 ± 1.1 , 30.7 ± 1.2 K and a FIR luminosity of $10^{7.91 \pm 0.02}$, $10^{8.13 \pm 0.03}$, $10^{8.71 \pm 0.03}$ L_{\odot} for NGC 4636, NGC 5846 and NGC 5044 respectively. The faint NGC 4636 ALMA continuum is in good agreement with the expected emission from cold dust, which would indicate that the dust content of NGC 4636 is fairly centrally located. The stronger continuum from NGC 5846 and NGC 5044 is an order of magnitude larger than the expected emission from cold dust or synchrotron. This strong continuum could be due to free-free emission from HII regions which can dominate in the 30 to 200 GHz range. However, these results are somewhat weakened by the fact that some of these observations were performed at difference scales. Given FIR fluxes were measured on a larger scale than ALMA fluxes, cold dust emission could not contribute more to ALMA fluxes for NGC 5846 and NGC 5044, but the synchrotron contribution could be larger or lower depending on the model adopted to match the observed scales. It is also not possible to exclude that NGC 4636 ALMA flux could be a combination of synchrotron and dust emission, even if it matches the cold dust SED. New radio observations matching ALMA PSF would allow to improve this analysis.

5.2. Kinematics interpretation

Cloud #1 and #3 of NGC 5846 are resolved and have an average radius ($r_c = \sqrt{\sigma_{\text{maj}} \sigma_{\text{min}}}$) of $0.21'' \pm 0.11''$ and $0.61'' \pm 0.04''$ respectively (see Table 4). For these clouds, we calculate

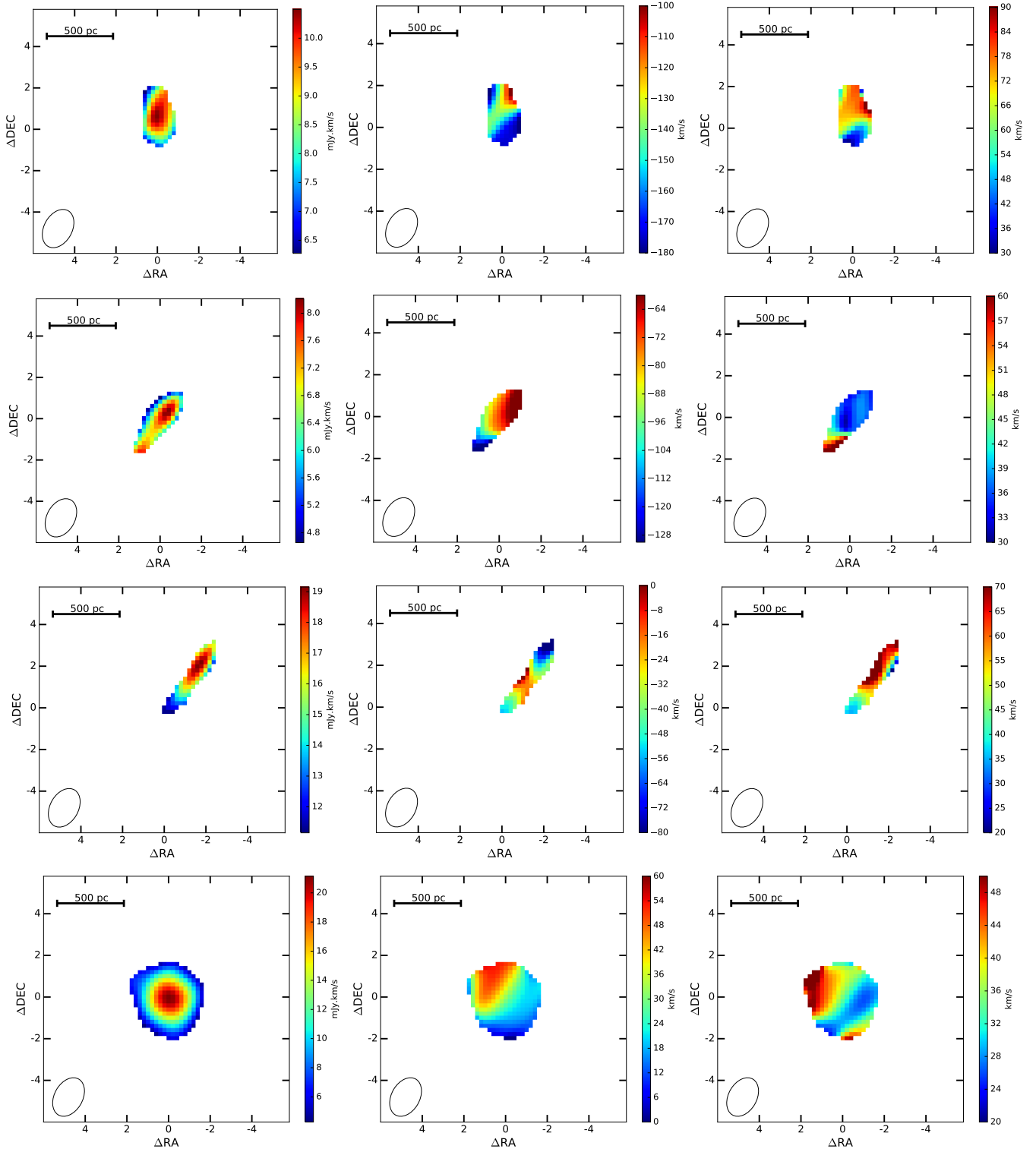


Figure 8. Flux (left), velocity (center) and velocity dispersion (right) in cloud #8,13,14,18 of NGC 5044. The flux image has been calculated by integrating the signal 3σ around the peak, flux errors are typically about 1 mJy km s^{-1} (except for cloud #13 where it is 4 mJy km s^{-1}). Velocity and velocity dispersion have been obtained by fitting the emission line and have typical uncertainty of km s^{-1} . The ellipse in the left bottom corner represents ALMA beam size.

the surface mass density that is respectively 460 ± 332 and $39 \pm 4 \text{ M}_{\odot} \text{ pc}^{-2}$ and the n_{H_2} volume densities are respectively 274 ± 240 and $8.0 \pm 1.0 \text{ cm}^{-3}$. NGC 5044 clouds have an average radius between 79 and 139 pc, a surface mass density of 56 ± 24 , 75 ± 56 , 76 ± 43 and $476 \pm 214 \text{ M}_{\odot} \text{ pc}^{-2}$ and a n_{H_2} vol-

ume density of 6 ± 3 , 11 ± 10 , $10 \pm$ and $89 \pm 49 \text{ cm}^{-3}$ for cloud #8,12,13,15 respectively. The large uncertainty of these values is due to the fact that the minor axis of all the clouds is very close to the size of the beam, the deconvolved value of the minor axis (σ_{min}) is therefore very small and has a large relative uncertainty. The lower uncertainty on cloud #3 is due

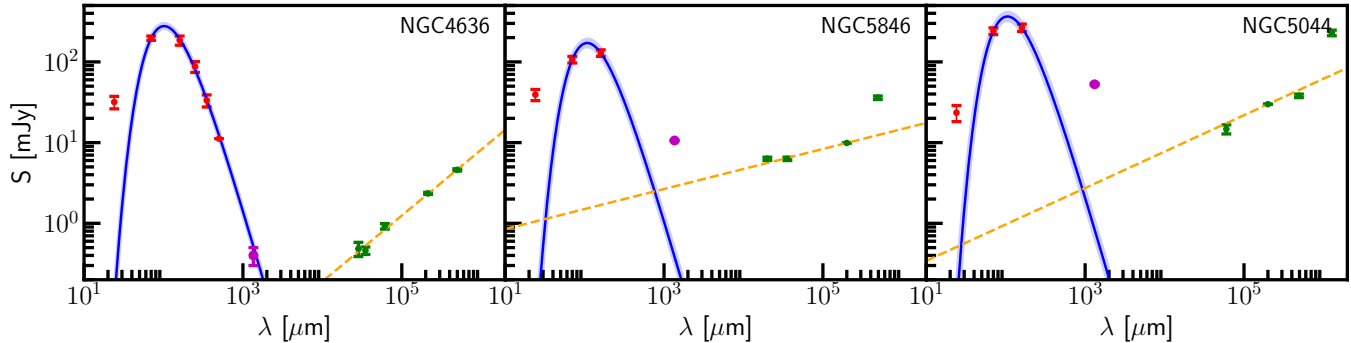


Figure 9. FIR to radio spectra of NGC 4636 (left), NGC 5846 (center) and NGC 5044 (right). Red circles represent data from *Spitzer*-MIPS and *Herschel*-SPIRE (NGC 4636), green circles represent radio measurements, magenta circles represent our ALMA continuum measurements. The blue line is a modified black-body (emissivity $\beta=1.5$) fit to data in the $70\mu\text{m}$ - $500\mu\text{m}$ range, the light blue shade represents its uncertainty. The orange dashed line is a fit to the radio data by a power-law spectrum.

ID	r_c (pc)	Σ ($M_\odot \text{ pc}^{-2}$)	n_{H_2} (cm^{-3})	α
NGC 5846				
1	24.8 ± 12.6	460.2 ± 331.9	274.2 ± 241.7	18.0 ± 9.4
3	72.2 ± 4.3	39.1 ± 4.1	8.0 ± 1.0	53.0 ± 7.7
NGC 5044				
8	139.0 ± 41.8	55.9 ± 24.3	5.9 ± 3.1	283.8 ± 96.9
13	104.8 ± 54.2	75.4 ± 55.6	10.6 ± 9.6	89.2 ± 52.6
14	113.1 ± 41.4	76.4 ± 43.4	10.0 ± 6.8	66.8 ± 35.2
18	79.2 ± 25.1	476.1 ± 214.2	88.9 ± 48.9	14.1 ± 4.6

Table 4

Cloud radius, surface mass density, volume density and virial factor for the 2 resolved clouds of NGC 5846 and the 4 resolved clouds of NGC 5044.

to the fact that we are using the convolved value of its dimension since we could not deconvolve the value of its minor axis.

To derive whether these molecular associations are gravitationally bounded, we can calculate the virial parameters from Bertoldi & McKee (1992):

$$\alpha = \frac{5\sigma^2 R}{GM} \quad (2)$$

A virial parameter ~ 1 indicates that a cloud is gravitationally bound, while a virial parameter $\gg 1$ indicates that a cloud is unbound or pressure bound. All the detected and resolved clouds have a virial parameter much $\gg 1$ (see Table 2), although with large uncertainties (due to large errors in the cloud radii). Deeper observations with a better PSF could allow to more properly resolve each clumps, and potentially detect sub-components with thinner CO lines. These sub-components could have a smaller virial parameters. Indeed the large virial parameters might indicate that the clouds in NGC 5846 and NGC 5044 are unbound giant molecular associations drifting in the turbulent velocity field (dominated by the large eddies at kpc scale) and which may disperse in a relatively short timescale $r_c/\sigma \approx 1-10$ Myr. Alternatively, the large CO linewidths may arise in molecular gas flowing out from clouds surfaces due to heating by the local hot gas atmosphere. Deeper observations with a smaller PSF are needed to better characterize the CO clumps detected in these observations.

6. DISCUSSION

Our new observations and detection of CO emitting clouds in NGC 5846 and NGC 4636 confirm the presence of molecular gas in group centered galaxies in the form of compact clouds. A diffuse CO component, if present, has not been detected by our ACA observations in these two galaxies. Previous attempts of detecting diffuse molecular gas with single dish observations have failed as well (Combes, IRAM observations).

Because of the angular sensitivity of interferometric measurements, ALMA observations are sensitive to emission in a selected range of angular scales. At the scale distance of galaxy groups, ALMA observations preferentially detect individual clouds, which may comprise a small fraction of the total molecular mass. In more distant clusters, where the ALMA beam size is of the order of few kpc, the maximum recoverable size becomes a good match for detecting the diffuse emission (David et al. 2017).

It is worth to note that molecular gas masses reported in Table 3 have been evaluated assuming the conversion between CO luminosity and H_2 mass derived for our Galaxy or other normal star-forming galaxies. However, such conversion factor may not be appropriate for massive elliptical galaxies at the center of groups and clusters (Lim et al. 2017, and references therein). The environment in which the molecular gas is immersed in massive ellipticals strongly constrains and defines the physical parameters of the molecular gas and it differs substantially from the surrounding ambient of Galactic GMCs. The Galactic X_{CO} may overpredict the mass of CO clouds in this very different group environment where the CO line emissivity may be unusually large. Using ALMA observations of CO(3-2) and ^{13}CO (3-2) in the brightest cluster galaxy of RXJ0821+0752, Vantyghem et al. (2017) have estimated that the galactic X_{CO} factor overestimates the true molecular mass by a factor of two.

There is mounting evidence that the molecular gas in these systems cooled from the hot interstellar or intragroup medium (e.g. Hogan et al. 2017; Pulido et al. 2017, and references therein).

A remarkable observational result is the cospatiality among the different gas phases that extend to the observed filamentary structures of each gaseous component. For instance, the X-ray emission is highly cospatial with the optical, infrared, and radio emission of cold/warm gas (e.g. Werner et al. 2014). The [CII] emission, thought to originate in warm gas that roughly moves with the hot gas, correlates well with the $\text{H}\alpha$ + [NII] emission, and in all three galaxies, the [CII]/ $\text{H}\alpha$ + [NII] ratio remains relatively constant with total luminosity ratio ~ 0.6 (Werner et al. 2014), corroborating the

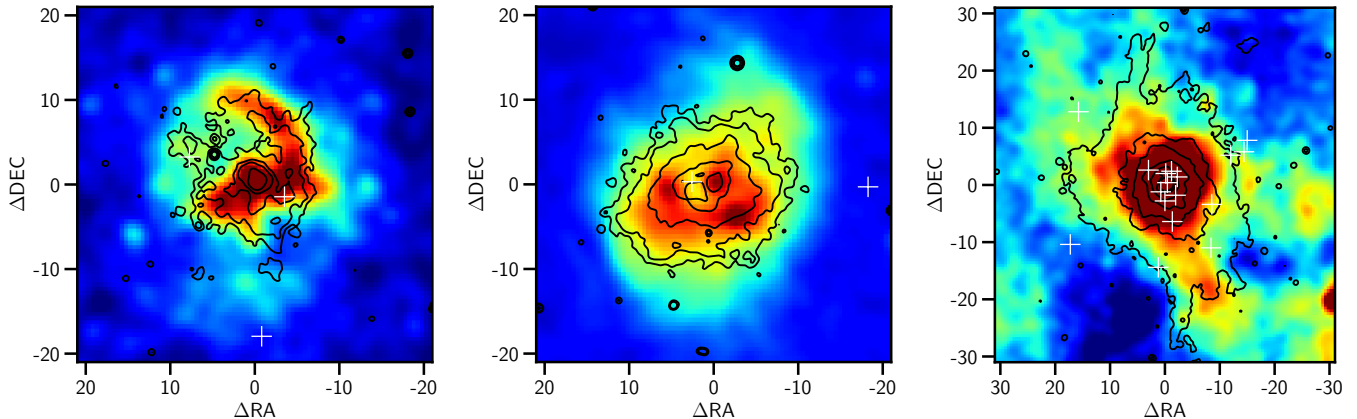


Figure 10. *Chandra* images of NGC 5846, NGC 4636 and NGC 5044 with superimposed contours of their respective $H\alpha+[NII]$ emission. An excellent correlation is apparent in the central region as well as in the extended filamentary structures of the three galaxies. White crosses mark the detected CO cloud positions.

scenario of in-situ gas condensation via nonlinear thermal instability. Dust absorption features in the optical HST images show a good correlation with the central $H\alpha+[NII]$ emission and filamentary structures (see Figure 2 and 3).

In addition multi-wavelength observations indicate that the presence of a multiphase ISM strongly correlates with the hot atmosphere properties, such as short cooling time ($t_{\text{cool}} \lesssim 3 \times 10^8$ yr), low entropy parameter ($kT/n^{2/3} \lesssim 15$ keV cm²), small cooling time to dynamical time ratio ($t_{\text{cool}}/t_{\text{dyn}} \lesssim 20$), and $t_{\text{cool}}/t_{\text{eddy}} \approx 1$. Early 2D hydrodynamic simulations of AGN heated galaxy group atmospheres (Brighenti & Mathews 2002) suggested that spatially distributed cooling in localized compressed regions, where nonlinear density perturbations cools rapidly to $T \lesssim 5 \times 10^4$ K. In recent years much progress has been made in our understanding of the heating/cooling cycle in galaxies and clusters (Revaz et al. 2008; McCourt et al. 2012; Sharma et al. 2012; Gaspari et al. 2012, 2013, 2017a,b; Li & Bryan 2014; Li et al. 2015; Brighenti et al. 2015; Valentini & Brighenti 2015; Voit et al. 2017). These studies have shown that cooling perturbations can be generated by several sources, like turbulence (e.g. Gaspari et al. 2012), AGN outflows (e.g. Gaspari et al. 2011), or buoyant cavities (e.g. Brighenti et al. 2015). The latter two mechanisms are particularly effective in stimulating cooling because they cause some of the low entropy central gas to be transported to larger radii (albeit only along a preferential direction), where the dynamical time is larger (see also McNamara et al. 2016).

However, a general prediction for these cooling scenarios is that the cold gas should be dust poor (e.g. Valentini & Brighenti 2015, and references therein), although additional physics (as dust growth by accretion of gas-phase metals in the cold gas) may alter this outcome (Hirashita & Nozawa 2017). This prediction seems to be confirmed by our observation, where many CO clouds do not extinct background starlight, especially in NGC 5044, although given their small angular sizes, dusty clouds may not obscure much starlight. Thus, the exact alignment of NGC 5846 clouds #1 and #3 in Figure 2 with the dust suggests a further mechanism to form cold gas.

They could have only recently formed from relatively dust-rich gas produced by mixing dusty stellar mass loss or dusty warm gas originally present in the center of the galaxy and uplifted by the AGN outburst with hot ISM. Dust-enhanced

cooling can easily cool hot gas on time scales less than the local freefall time (Mathews & Brighenti 2003). Another possible origin for orbiting dusty molecular clouds is direct acceleration of molecular gas present in the central region. However, as discussed by McNamara et al. (2016) and references therein, it is unclear how low-density jets or buoyant cavities can drag very dense and compact clouds to height of several kpc.

More distant CO clouds, like Cloud #2 in N5846, not associated with gas having an enhanced dust/gas ratio, are thought to originate from cooling in the wakes beneath buoyant X-ray cavities where compressions stimulate significant large-scale, coherent radiative cooling (Brighenti et al. 2015; Valentini & Brighenti 2015).

The tight spatial correlation between the soft X-ray and warm gas emission (Figure 10), together with the cold molecular gas, is an important clue that the multiphase gas arises from the top-down nonlinear condensation process (Gaspari et al. 2017a), i.e., cascading from the turbulent hot plasma to warm filaments and to the molecular clouds at the overdensity peaks. The high-resolution 3D simulations in Gaspari et al. (2017a,b) allow a quantitative comparison with the observations presented here. Gaspari et al. (2017a,b) show that the cold clouds often agglomerate in giant molecular associations (sometime in projection), which are not virialized, but rather characterized by significant velocity dispersion (and thus virial parameter $\alpha \gg 1$). Typical properties of simulated clouds (related to the high-end tail of the molecular gas distribution) are masses in the range $10^4 - 10^6 M_{\odot}$ and effective radii 50 - 250 pc, which are well consistent with the observational data. The simulations also predict several smaller and less massive clouds, which can not be detected by our observations.

Analysis of the kinematics of the multiphase gas, in long-term AGN jet feedback simulations runs (Gaspari et al. 2017a), reveals that warm and cold gas are – as ensemble – robust kinematic tracers of the turbulent hot gas. This is substantiated by multi-wavelength observations of NGC 5044. The ensemble velocity dispersion for NGC 5044 molecular clouds (which can be approximated via the RMS of the velocity offsets; Tab. 3) is $\sigma_{v,\text{los,ens}} \simeq 177$ km s⁻¹. The velocity dispersion from $H\alpha+[NII]$ data results to be 190 km s⁻¹ (Gaspari et al. 2017a). The two are comparable (errors are $\lesssim 10$ km s⁻¹) and very similar to the hot plasma value

of 172 km s^{-1} (Ogorzalek et al. 2017). Unfortunately, for NGC 4636 and NGC 5846 the small number of clouds detected prevent a similar analysis. Gaspari et al. (2017a) runs also show that, due to the turbulence cascade ($\sigma_v \propto l^{1/3}$), the small-scale structures typically have low velocity dispersion ($< 100 \text{ km s}^{-1}$) but large velocity shift, up to several 100 km s^{-1} , in agreement with our observational findings (Sec. 4-5 and Tab. 3).

Overall, the consistent results between the numerical predictions and the observational findings – e.g., the cospatiality among the soft X-ray, optical/IR and radio structures, the correlation with short plasma cooling times, the large virial parameter, the masses and radii of the clouds, the tightly linked ensemble kinematics among all the phases (X-ray, H α + [NII], [CII], CO), and the cloud σ_v tracing the turbulent cascade – they all corroborate the important role that the top-down condensation cascade and related CCA play in shaping the multiphase halos of massive galaxies, groups, and clusters.

The broad CO line widths of the molecular clouds in these galaxies, which would imply that are unbound systems, is of particular interest. The large CO linewidths may arise in gas flowing out from clouds surfaces due to heating by the local hot gas atmosphere. Broad, rather symmetric CO line profiles are formed by the combined emission from outflows on both the near and far cloud surfaces. Fast CO outflows also guarantee that CO lines are absorbed locally; doppler-shifted CO line radiation from distant surfaces will not be absorbed. Furthermore, extreme CO outflow velocity gradients will sharply reduce optical depths in all CO lines and CO line emissivities may be greatly increased by collisional excitation at the relatively high temperature required to drive the observed expansion velocities. Future ALMA observations of CO at higher J transitions and proper knowledge of excitation mechanisms, would provide a better characterization of the physical properties of the molecular gas and the inferred gas mass.

7. CONCLUSIONS

We have presented new CO(2-1) ALMA observations of two group centered elliptical galaxies, NGC 5846 and NGC 4636. With the addition of the revised cycle 0 observations of NGC 5044, we have confirmation that CO molecular clouds are common features in these massive ellipticals. Our main results are summarized as follows.

- The off-center orbiting clouds exhibit CO linewidths that are $\gtrsim 10$ times broader than Galactic molecular clouds. The associated total molecular mass ranges from $2.6 \times 10^5 M_\odot$ in NGC 4636 to $6.1 \times 10^7 M_\odot$ in NGC 5044. These masses have been estimated assuming the CO-to-H $_2$ conversion factor calibrated for the Milky Way and nearby spiral galaxies. Since significant deviations from the Galactic X_{CO} are observed in other galaxies (Vantyghem et al. 2017), it is expected that the presented molecular masses are overestimated. A diffuse CO component, if present, has not been detected at the sensitivity level of our ACA observations in NGC 5846 and NGC 4636. It is worth to note that given the angular sensitivity of interferometric measurements, ALMA observations at a distance scale of local groups preferentially detect individual clouds, which may account for a small fraction of the total molecular mass.

- The origin of the detected molecular features is still uncertain, but there is evidence that the molecular gas has cooled from the hot gas. The observed spatial and kinematical correlation among the different phases - hot (soft X-ray), warm (H α), cold ([CII]), and molecular (CO) - of the multiphase gas in the atmosphere of these galaxies, support the scenario of in-situ condensation, as opposed to gas stripping from merging galaxies. Also, the hot atmosphere properties - short cooling time, low entropy parameter, and small cooling time to dynamical/eddy time ratio - are consistent with the necessary conditions to promote gas cooling via thermal instabilities, as predicted by hydrodynamic simulations.

The central CO clouds in strong spatial correlation with dust (e.g. cloud #1 and #3 in NGC 5846) may have recently formed and cooled from the hot gas phase via dust-enhanced cooling. The global condensation mechanism can be triggered via nonlinear perturbations generated in the chaotic turbulent velocity field or during the bubble uplift.

- The large virial parameter of the molecular structures, their large CO(2-1) line widths, and correlation with the warm/hot phase kinematics provide evidence that they are unbound giant molecular associations drifting in the turbulent field, consistently with numerical predictions of the CCA process. Alternatively, the observed large CO line widths may be generated by molecular gas flowing out from cloud surfaces due to heating by the local hot gas atmosphere.

Despite the uncertainties listed above, we expect the surfaces of CO-emitting clouds in galaxy group environments to be strongly heated by their environment. This heating is expected to excite higher rotational J-levels with high CO emissivity. Future ALMA observations of CO line fluxes at higher J-levels in these galaxy groups will be critical for our understanding of the formation and evolution of such clouds.

ACKNOWLEDGEMENTS

This paper makes use of the following ALMA data: ADS/JAO.ALMA#2015.1.00860.S, ADS/JAO.ALMA#2011.0.00735.SSB. ALMA is a partnership of ESO (representing its member states), NSF (USA) and NINS (Japan), together with NRC (Canada), MOST and ASIAA (Taiwan), and KASI (Republic of Korea), in cooperation with the Republic of Chile. The Joint ALMA Observatory is operated by ESO, AUI/NRAO and NAOJ. The National Radio Astronomy Observatory is a facility of the National Science Foundation operated under cooperative agreement by Associated Universities, Inc. Massimo Gaspari is supported by NASA through Einstein Postdoctoral Fellowship Award Number PF5-160137 issued by the Chandra X-ray Observatory Center, which is operated by the SAO for and on behalf of NASA under contract NAS8-03060. Support for this work was also provided by Chandra grant GO7-18121X. HPC resources were in part provided by the NASA/Ames HEC Program (SMD-16-7320, SMD-16-7321, SMD-16-7305). Myriam Gitti thanks the Italian ARC staff in Bologna, in particular E. Liuzzo and M. Massardi, for their helpful advice during the data reduction. Myriam Gitti acknowledges partial support from PRIN-INAF 2014.

REFERENCES

- Allen S. W., Dunn R. J. H., Fabian A. C., Taylor G. B., Reynolds C. S., 2006, *MNRAS*, **372**, 21
- Amblard A., Riguccini L., Temi P., Im S., Fanelli M., Serra P., 2014, *ApJ*, **783**, 135
- Anderson M. E., Gaspari M., White S. D. M., Wang W., Dai X., 2015, *MNRAS*, **449**, 3806
- Annibali F., Bressan A., Rampazzo R., Zeilinger W. W., 2006, *A&A*, **445**, 79
- Baldi A., Forman W., Jones C., Kraft R., Nulsen P., Churazov E., David L., Giacintucci S., 2009, *ApJ*, **707**, 1034
- Barai P., Murante G., Borgani S., Gaspari M., Granato G. L., Monaco P., Ragone-Figueroa C., 2016, *MNRAS*, **461**, 1548
- Bertoldi F., McKee C. F., 1992, *ApJ*, **395**, 140
- Bolatto A. D., Wolfire M., Leroy A. K., 2013, *ARA&A*, **51**, 207
- Braine J., Combes F., 1992, *A&A*, **264**, 433
- Bregman J. N., Miller E. D., Irwin J. A., 2001, *ApJ*, **553**, L125
- Bregman J. N., Miller E. D., Athey A. E., Irwin J. A., 2005, *ApJ*, **635**, 1031
- Brighenti F., Mathews W. G., 2002, *ApJ*, **573**, 542
- Brighenti F., Mathews W. G., Temi P., 2015, *ApJ*, **802**, 118
- Caon N., Macchetto D., Pastoriza M., 2000, *ApJS*, **127**, 39
- Cappellari M., et al., 2011, *MNRAS*, **416**, 1680
- Cavagnolo K. W., McNamara B. R., Nulsen P. E. J., Carilli C. L., Jones C., Birzan L., 2010, *ApJ*, **720**, 1066
- Condon J. J., 1997, *PASP*, **109**, 166
- Croton D. J., et al., 2006, *MNRAS*, **365**, 11
- Daddi E., et al., 2005, *ApJ*, **626**, 680
- David L. P., et al., 2014, *ApJ*, **792**, 94
- David L. P., Vrtilik J., O'Sullivan E., Jones C., Forman W., Sun M., 2017, *ApJ*, **842**, 84
- Davis T. A., et al., 2011, *MNRAS*, **417**, 882
- Diniz S. I. F., Pastoriza M. G., Hernandez-Jimenez J. A., Riffel R., Ricci T. V., Steiner J. E., Riffel R. A., 2017, *MNRAS*, **470**, 1703
- Edge A. C., 2001, *MNRAS*, **328**, 762
- Emsellem E., et al., 2011, *MNRAS*, **414**, 888
- Fabian A. C., 2012, *ARA&A*, **50**, 455
- Feldmann R., Carollo C. M., Mayer L., Renzini A., Lake G., Quinn T., Stinson G. S., Yepes G., 2010, *ApJ*, **709**, 218
- Filho M. E., Fraternali F., Markoff S., Nagar N. M., Barthel P. D., Ho L. C., Yuan F., 2004, *A&A*, **418**, 429
- Gaspari M., Sądowski A., 2017, *ApJ*, **837**, 149
- Gaspari M., Melioli C., Brighenti F., D'Ercole A., 2011, *MNRAS*, **411**, 349
- Gaspari M., Brighenti F., Temi P., 2012, *MNRAS*, **424**, 190
- Gaspari M., Ruszkowski M., Oh S. P., 2013, *MNRAS*, **432**, 3401
- Gaspari M., Brighenti F., Temi P., 2015, *A&A*, **579**, A62
- Gaspari M., et al., 2017a, preprint, ([arXiv:1709.06564](https://arxiv.org/abs/1709.06564))
- Gaspari M., Temi P., Brighenti F., 2017b, *MNRAS*, **466**, 677
- Giacintucci S., et al., 2011, *ApJ*, **732**, 95
- Gitti M., Brighenti F., McNamara B. R., 2012, *Advances in Astronomy*, **2012**, 950641
- Goulding A. D., et al., 2016, *ApJ*, **826**, 167
- Gozaliasl G., Finoguenov A., Khosroshahi H. G., Mirkazemi M., Erfanianfar G., Tanaka M., 2016, *MNRAS*, **458**, 2762
- Haardt F., Madau P., 2012, *ApJ*, **746**, 125
- Hirashita H., Nozawa T., 2017, preprint, ([arXiv:1701.07200](https://arxiv.org/abs/1701.07200))
- Hogan M. T., McNamara B. R., Pulido F., Nulsen P. E. J., Russell H. R., Vantghem A. N., Edge A. C., Main R. A., 2017, *ApJ*, **837**, 51
- Jones C., Forman W., Vikhlinin A., Markevitch M., David L., Warmflash A., Murray S., Nulsen P. E. J., 2002, *ApJ*, **567**, L115
- Lau E. T., Gaspari M., Nagai D., Coppi P., 2017, preprint, ([arXiv:1705.06280](https://arxiv.org/abs/1705.06280))
- Li Y., Bryan G. L., 2014, *ApJ*, **789**, 54
- Li Y., Bryan G. L., Ruszkowski M., Voit G. M., O'Shea B. W., Donahue M., 2015, *ApJ*, **811**, 73
- Lim J., Dinh-V-Trung Vrtilik J., David L. P., Forman W., 2017, preprint, ([arXiv:1710.06186](https://arxiv.org/abs/1710.06186))
- Machacek M. E., Jerius D., Kraft R., Forman W. R., Jones C., Randall S., Giacintucci S., Sun M., 2011, *ApJ*, **743**, 15
- Mahdavi A., Trentham N., Tully R. B., 2005, *AJ*, **130**, 1502
- Mathews W. G., Brighenti F., 2003, *ApJ*, **590**, L5
- Mathews W. G., Temi P., Brighenti F., Amblard A., 2013, *ApJ*, **768**, 28
- McCourt M., Sharma P., Quataert E., Parrish I. J., 2012, *MNRAS*, **419**, 3319
- McDonald M., Veilleux S., Mushotzky R., 2011, *ApJ*, **731**, 33
- McMullin J. P., Waters B., Schiebel D., Young W., Golap K., 2007, in Shaw R. A., Hill F., Bell D. J., eds, *Astronomical Society of the Pacific Conference Series Vol. 376, Astronomical Data Analysis Software and Systems XVI*. p. 127
- McNamara B. R., Nulsen P. E. J., 2007, *ARA&A*, **45**, 117
- McNamara B. R., Nulsen P. E. J., 2012, *New Journal of Physics*, **14**, 055023
- McNamara B. R., Russell H. R., Nulsen P. E. J., Hogan M. T., Fabian A. C., Pulido F., Edge A. C., 2016, *ApJ*, **830**, 79
- Mei S., et al., 2007, *ApJ*, **655**, 144
- Merritt D., Ferrarese L., 2001, *MNRAS*, **320**, L30
- Molendi S., Tozzi P., Gaspari M., De Grandi S., Gastaldello F., Ghizzardi S., Rossetti M., 2016, *A&A*, **595**, A123
- Nagar N. M., Falcke H., Wilson A. S., 2005, *A&A*, **435**, 521
- O'Sullivan E., Combes F., Hamer S., Salomé P., Babul A., Raychaudhury S., 2015, *A&A*, **573**, A111
- O'Sullivan E., et al., 2017, *MNRAS*, **472**, 1482
- Ogorzalek A., et al., 2017, preprint, ([arXiv:1702.04364](https://arxiv.org/abs/1702.04364))
- Peterson J. R., Fabian A. C., 2006, *Phys. Rep.*, **427**, 1
- Peterson J. R., Kahn S. M., Paerels F. B. S., Kaastra J. S., Tamura T., Bleeker J. M., Ferrigno C., Jernigan J., 2003, *ApJ*, **590**, 207
- Pulido F. A., et al., 2017, preprint, ([arXiv:1710.04664](https://arxiv.org/abs/1710.04664))
- Rampazzo R., Panuzzo P., Vega O., Marino A., Bressan A., Clemens M. S., 2013, *MNRAS*, **432**, 374
- Revaz Y., Combes F., Salomé P., 2008, *A&A*, **477**, L33
- Salomé P., Combes F., 2003, *A&A*, **412**, 657
- Sarzi M., et al., 2013, *MNRAS*, **432**, 1845
- Sharma P., McCourt M., Quataert E., Parrish I. J., 2012, *MNRAS*, **420**, 3174
- Smith D. J. B., et al., 2012, *MNRAS*, **427**, 703
- Sun M., 2012, *New Journal of Physics*, **14**, 045004
- Temi P., Brighenti F., Mathews W. G., 2007a, *ApJ*, **660**, 1215
- Temi P., Brighenti F., Mathews W. G., 2007b, *ApJ*, **666**, 222
- Temi P., Brighenti F., Mathews W. G., 2009, *ApJ*, **695**, 1
- Tonry J. L., Dressler A., Blakeslee J. P., Ajhar E. A., Fletcher A. B., Luppino G. A., Metzger M. R., Moore C. B., 2001, *ApJ*, **546**, 681
- Trager S. C., Faber S. M., Worthey G., González J. J., 2000, *AJ*, **120**, 165
- Trinchieri G., Goudfrooij P., 2002, *A&A*, **386**, 472
- Valentini M., Brighenti F., 2015, *MNRAS*, **448**, 1979
- Vantghem A. N., et al., 2017, *ApJ*, **848**, 101
- Voit G. M., Donahue M., Bryan G. L., McDonald M., 2015, *Nature*, **519**, 203
- Voit G. M., Meece G., Li Y., O'Shea B. W., Bryan G. L., Donahue M., 2017, *ApJ*, **845**, 80
- Vollmer B., Thierbach M., Wielebinski R., 2004, *A&A*, **418**, 1
- Werner N., et al., 2014, *MNRAS*, **439**, 2291
- Ziegler B. L., Thomas D., Böhm A., Bender R., Fritz A., Maraston C., 2005, *A&A*, **433**, 519
- van der Wel A., Franx M., van Dokkum P. G., Rix H.-W., Illingworth G. D., Rosati P., 2005, *ApJ*, **631**, 145